

RESEARCH ARTICLE

10.1029/2018JA025820

Key Points:

- Derivation of energetic ion moments, κ -index, characteristic energy, temperature, and polytropic index in Saturn's magnetosphere
- Presentation of a semiempirical analytical model for the 20 keV energetic ion Pressure, density, and temperature
- The neutral gas at Saturn provides an effective cooling mechanism and does not allow the plasma sheet to behave adiabatically

Correspondence to:

K. Dialynas,
kdialynas@phys.uoa.gr

Citation:

Dialynas, K., Roussos, E., Regoli, L., Paranicas, C. P., Krimigis, S. M., Kane, M., et al. (2018). Energetic ion moments and polytropic index in Saturn's magnetosphere using Cassini/MIMI measurements: A simple model based on κ -distribution functions. *Journal of Geophysical Research: Space Physics*, 123, 8066–8086. <https://doi.org/10.1029/2018JA025820>



Received 25 JUN 2018

Accepted 11 SEP 2018

Accepted article online 17 SEP 2018

Published online 2 OCT 2018

Energetic Ion Moments and Polytropic Index in Saturn's Magnetosphere using Cassini/MIMI Measurements: A Simple Model Based on κ -Distribution Functions

Konstantinos Dialynas¹ , Elias Roussos² , Leonardo Regoli³ , Christopher P. Paranicas⁴ , Stamatios M. Krimigis^{1,4}, Mark Kane⁵ , Donald G. Mitchell⁴ , Douglas C. Hamilton⁶, Norbert Krupp² , and James F. Carbary⁴

¹Office of Space Research and Technology, Academy of Athens, Athens, Greece, ²Max-Planck-Institut für Sonnensystemforschung, Göttingen, Germany, ³Department of Climate, Space sciences & Engineering, University of Michigan, Ann Arbor, MI, USA, ⁴Applied Physics Laboratory, Johns Hopkins University, Baltimore, MD, USA, ⁵Harford Research Institute, MD, USA, ⁶Department of Physics, University of Maryland, College Park, MD, USA

Abstract Moments of the charged particle distribution function provide a compact way of studying the transport, acceleration, and interactions of plasma and energetic particles in the magnetosphere. We employ κ -distributions to describe the energy spectra of H^+ and O^+ , based on >20 keV measurements by the three detectors of Cassini's Magnetospheric Imaging Instrument, covering the time period from DOY 183/2004 to 016/2016, $5 < L < 20$. From the analytical spectra we calculate the equatorial distributions of energetic ion moments inside Saturn's magnetosphere and then focus on the distributions of the characteristic energy ($E_c = I_E/I_n$), temperature, and κ -index of these ions. A semiempirical model is utilized to simulate the equatorial ion moments in both local time and L-shell, allowing the derivation of the polytropic index (Γ) for both H^+ and O^+ . Primary results are as follows: (a) The $\sim 9 < L < 20$ region corresponds to a local equatorial acceleration region, where subadiabatic transport of H^+ ($\Gamma \sim 1.25$) and quasi-isothermal behavior of O^+ ($\Gamma \sim 0.95$) dominate the ion energetics; (b) energetic ions are heavily depleted in the inner magnetospheric regions, and their behavior appears to be quasi-isothermal ($\Gamma < 1$); (c) the (quasi-) periodic energetic ion injections in the outer parts of Saturn's magnetosphere (especially beyond $17-18 R_S$) produce durable signatures in the energetic ion moments; (d) the plasma sheet does not seem to have a *ground thermodynamic state*, but the extended neutral gas distribution at Saturn provides an effective cooling mechanism that does not allow the plasma sheet to behave adiabatically.

1. Introduction

The inner to middle magnetosphere of Saturn ($<10 R_S$, $1 R_S = 60,268$ km) forms a very diverse region where the charged particles coexist with the planetary ring system, dust, the inner satellites, the neutral gas cloud, and the radiation belts. The dominant species in both the thermal (Young et al., 2005) and suprathermal (Krimigis et al., 2005) energy range out to $\sim 10 R_S$ are protons (H^+) and water group ions (O^+ , H_2O^+ , OH^+). Depending on the energies considered, these species may originate from the rings (e.g., Christon et al., 2013), galactic cosmic ray secondaries (Roussos et al., 2011), and icy satellites through sputtering (Johnson et al., 2008). Further, a significant amount of atomic hydrogen has been found to originate from Saturn's top atmospheric layers (Shemansky et al., 2009). The small but noticeable percentage of He^{++} that was recently confirmed as well (Allen et al., 2018), which originates from the solar wind, is possibly indicative of the solar wind-magnetosphere coupling at Saturn.

However, when considering the global magnetospheric configuration and dynamics, these are only minor sources compared to Enceladus's contribution, located at $\sim 3.95 R_S$, that is, undeniably, the most prominent source of water group plasma inside the magnetosphere through its active cryovolcanoes (Dougherty et al., 2006; Porco et al., 2006; H. T. Smith et al., 2010). In both the inner and outer parts ($>10 R_S$) of the Saturnian system, neutral particles play a key role (Delamere et al., 2007; Dialynas et al., 2013) and even dominate the ion densities over a very broad magnetospheric region (Vasyliunas, 2008), acting as an effective source and loss mechanism of energetic ions (Paranicas et al., 2008).

The way(s) that these ions are distributed throughout the magnetosphere are key to establishing their source, loss, transport, and acceleration processes. From the perspective of energetic ions, heavy particles are usually

very reliable tracers of the different source and acceleration mechanisms acting inside the magnetosphere, which may involve complex effects (Mitchell et al., 2015) reflecting the magnetospheric dynamics: injections associated with plasma heating of inward moving flux tubes due to interchange instability (Kennelly et al., 2013), injections associated with current sheet collapse (Thomsen et al., 2013), inward radial diffusion (Roussos et al., 2007) involving adiabatic heating (Dialynas et al., 2009), or adiabatic energy loss with outward transport (Kane et al., 2014). Unlike protons, which may have multiple sources (e.g., solar wind, Enceladus, rings, ionosphere), the energetic O^+ is mainly sourced from the dissociation of H_2O from Enceladus. Further, it has been shown that O^+ occupies $\sim 50\%$ of the energetic particle pressure, while their contribution to the total pressure rapidly rises with increasing β ($=P_{plasma}/P_{magnetic}$), even becoming dominant for $\beta > 1$ (Sergis et al., 2007), thus exhibiting a significant participation in all the above mechanisms. Therefore, in the Magnetospheric Imaging Instrument (MIMI) energy range and measuring capabilities (see section 2) these ions may effectively trace the circulation and transport processes that lead to their acceleration.

For example, the acceleration of O^+ in rapid magnetic field reconfigurations has been shown to be associated with the breaking of its adiabatic invariants, because its gyroperiod and/or bounce period are too long compared to the reconfiguration time scales (unlike protons), leading to dramatic nonadiabatic acceleration. Such situations where protons and O^+ exhibit different behavior have been observed and explained at Saturn, in the region between 15 and 40 R_S (e.g., Carbary et al., 2008; Dialynas et al., 2009; Mitchell et al., 2005) and (especially) in Earth's magnetosphere (e.g., Delcourt, 2002; Fok et al., 2006). In addition, due to their large charge-exchange cross sections (Lindsay & Stebbings, 2005), the >20 keV O^+ lifetimes within the inner to middle magnetosphere are much shorter than the H^+ lifetimes in the same region, whereas the temperatures of energetic O^+ have been shown to be almost constant throughout the magnetosphere. This indicates that although adiabatic heating should take place for all particles inside the magnetosphere, little energy is gained as O^+ particles move toward the planet to stronger magnetic fields (Dialynas et al., 2009).

Here we focus on the spatial distributions of the >20 keV H^+ and O^+ moments that provide a compact way of characterizing some of the properties of different magnetospheric regions and give clues on the aforementioned processes. We perform our analyses using κ -distribution functions (cf. Livadiotis, 2017) that provide the framework for calculating physically meaningful parameters, such as the temperature, pressure, and density, together with their analytic representations. In conjunction, the κ -index is a very important parameter, since it is a prime indicator for systems that are not in local thermodynamic equilibrium and can be characterized as a source of *free energy* that can drive different plasma processes (Hapgood et al., 2011). The kappa function has been successfully used to fit both the low energy *thermal* parts and the flux excess of suprathermal ions since the Voyager era (e.g., Carbary et al., 1983; Krimigis et al., 1983) and recently using Cassini energetic ion measurements deep inside the magnetosphere (e.g., Dialynas et al., 2009; Kane et al., 2008), at the orbit of Titan (Regoli et al., 2018), and upstream of the Saturnian bow shock (Krimigis et al., 2009), but also neutral particle distributions (Jurac et al., 2002) and electrons (Carbary et al., 2011; Schippers et al., 2008).

The charged particle moments allow also the determination of the polytropic index that reveals the thermodynamic state of the Saturnian system, an important input for theoretical studies and modeling (e.g., Delamere et al., 2015, and references therein). Such an approach has been used successfully for the Earth's magnetosphere to calculate the polytropic index of the plasma sheet (e.g., Baumjohann & Paschmann, 1989; Huang et al., 1989) and the specific entropy (e.g., Borovsky & Cayton, 2011), and also in other space environments, such as the solar wind (Newbury et al., 1997) and the heliosheath (Livadiotis & McComas, 2012). Electron measurements with energies between 0.5 and 28 keV from Cassini suggested that Saturn's nightside plasma sheet behaves *isothermally*, as the polytropic index was found to be ~ 1 (Arridge et al., 2009).

The paper is organized as follows: In section 2 we describe the Cassini/MIMI instruments, the data sets, and measurement techniques used in this study. In section 3 we provide information on the ion spectral analyses and fits using κ -distribution functions, which are then employed to obtain equatorial distributions of the energetic ion moments (section 4). The equatorial distributions are then simulated (section 5) using a semiempirical, parametric model for the partial ion pressure (section 5.1), that is then used to simulate the energetic ion densities (section 5.2), obtaining the polytropic index for both H^+ and O^+ . The simulated pressure and density are then utilized to obtain the partial temperature (section 5.3), which also serves as a confirmation of the previous simulations. The shapes and general properties of all distributions are discussed throughout section 5. Section 6 includes a brief summary of the principal results of this study and is followed by

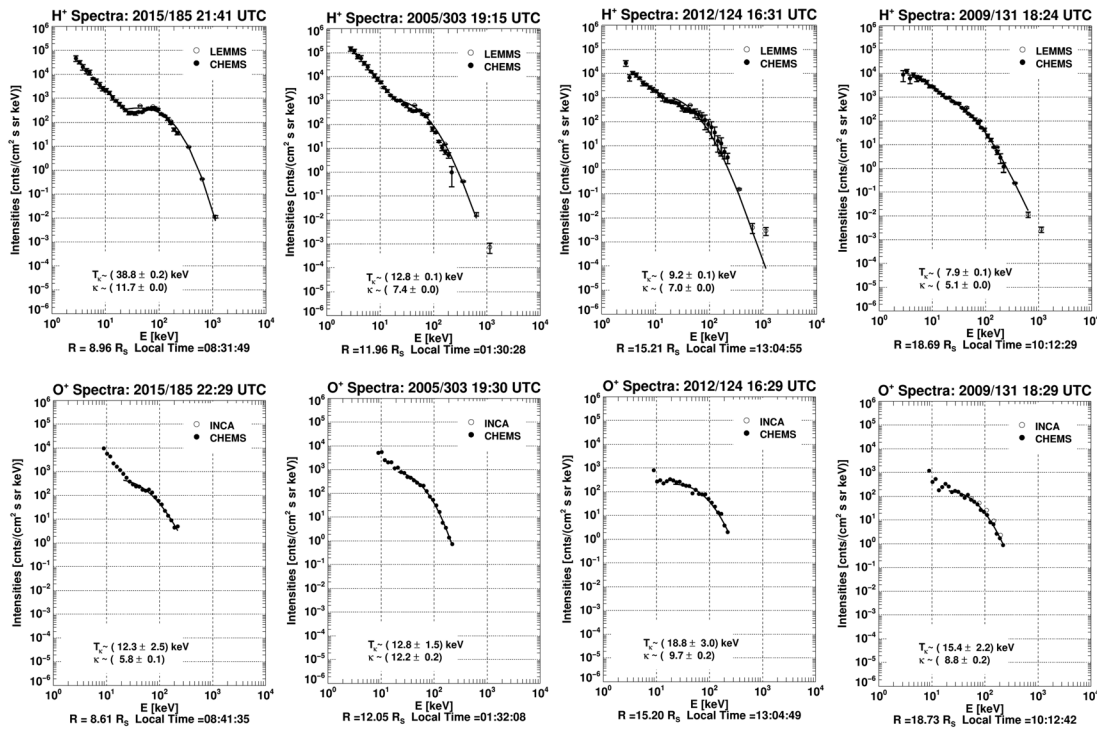


Figure 1. (top) Sampled proton spectra using combined CHEMS and LEMMS data in the energy range of ~ 3 keV to 2.3 MeV and (bottom) oxygen ion spectra using combined CHEMS-INCA data in the energy range of 9 to 677 keV over selected magnetospheric regions and different years. Fits to the >20 keV energy range with κ -distributions for both species (detailed in the text) are represented by the black solid lines. Measured uncertainties in intensities are comparable or smaller than the data points, unless otherwise noted. LEMMS = Low Energy Magnetospheric Measurement System; CHEMS = Charge Energy Mass Spectrometer; INCA = Ion Neutral Camera.

section 7 that provides a general discussion of our results concerning their consequences for the plasma sheet *thermodynamical* properties, in accordance with relevant studies found in the literature.

2. Instrumentation and Data Set Details

The MIMI experiment onboard Cassini consists of three independent particle detectors that provide both in situ particle and remote sensing measurements as explained by Krimigis et al. (2004). These detectors are the Low Energy Magnetospheric Measurement System (LEMMS), the Charge Energy Mass Spectrometer (CHEMS), and the Ion Neutral Camera (INCA).

Here we present a composite analysis of H^+ and O^+ to produce equatorial distributions using all available Cassini/MIMI data for the time period from the SOI (DOY 183/2004) to DOY 16/2016, and over a wide L-shell range of $5 < L < 20$. Due to differences in counting statistics, the accumulation time for H^+ (30 min) is different from O^+ (1 hr). The in situ ion data used in this study are a combination of CHEMS 3 to 226 keV/e channels for H^+ and 9 to 226 keV/e for O^+ , LEMMS A_0 – A_7 channels (assumed to be mostly counting protons) that cover the energy range of 30.7 keV to 2.3 MeV, and INCA Time-Of-Flight energy channels which occupy the 39 to 677 keV for O^+ , as explained by Dialynas et al. (2009). The CHEMS instrument measures water group ions (W^+) dominated by O^+ ($\sim 53\% O^+$, $\sim 22\% OH^+$, $\sim 22\% H_2O^+$, and $\sim 3\% H_3O^+$; DiFabio, 2012).

Owing to an on-demand voltage on its deflection plates, INCA can operate in two detection modes, namely *ion* and *neutral*. Because the primary purpose of INCA is to remotely image Saturn's magnetosphere, it does not always measure the O^+ distributions presented in Figure 1. On such occasions, we rely on the use of CHEMS data, and when CHEMS's rates are low, a reliable fit in the >20 keV O^+ energy spectra cannot be obtained, resulting in a gap in the equatorial distributions that we produce (e.g., see Figure 2). In the case of >20 keV H^+ , low CHEMS rates may be compensated by the LEMMS instrument, resulting in better data coverage than the O^+ .

In principle, the dayside plasma sheet extends up to $\pm 45^\circ$ latitude (Krimigis et al., 2007; Sergis et al., 2007), while the nightside plasma sheet is less extended ($\pm 10^\circ$ in latitude; Dialynas et al., 2013). Notably, the plasma

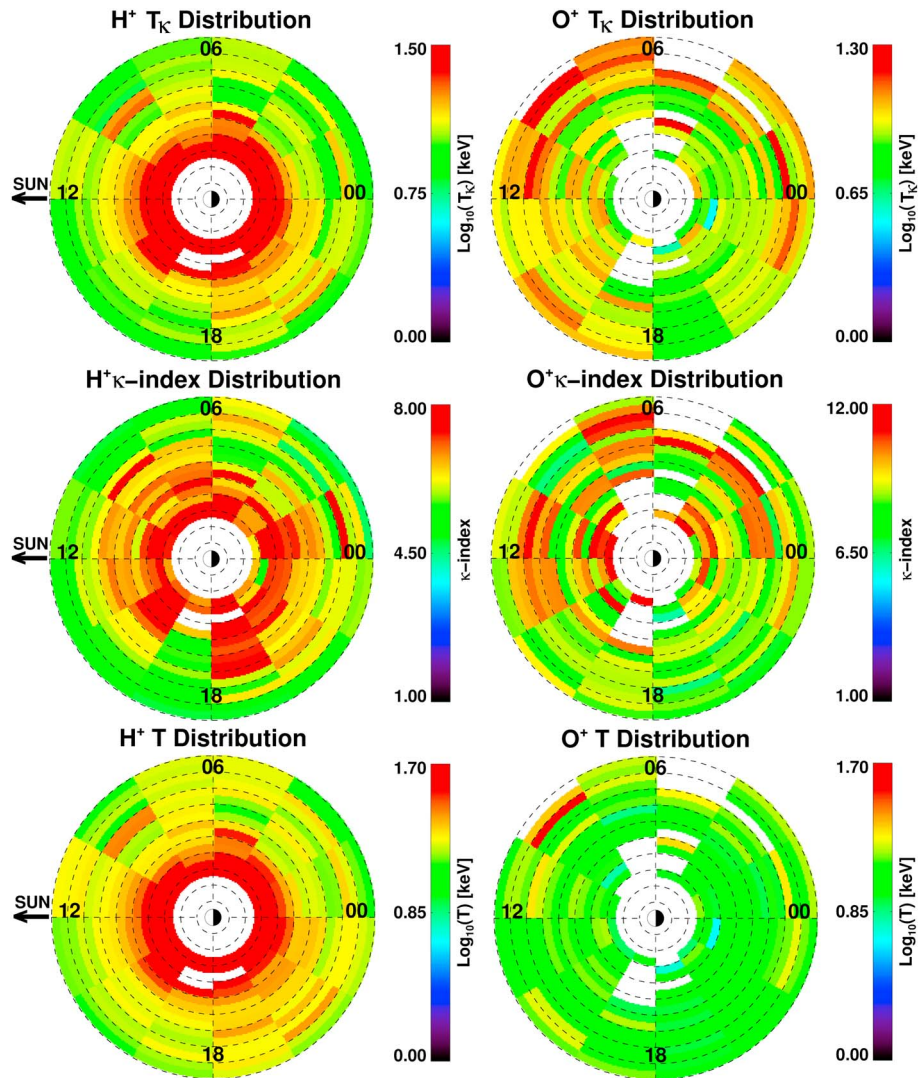


Figure 2. Color coded distributions of the fit parameters T_{κ} and κ -index, together with the equatorial distribution of T calculated from equation (2), for both H^+ (left row) and O^+ (right row) spectra in the region of $5 < L < 20$ mapped in the equatorial plane, as defined by the Khurana et al. (2006) model, with the precision afforded by our field line tracing procedure, less than $0.05 R_S$ in the Z -direction. The dashed circles denote the L -shells shown from the center of Saturn per $2 R_S$, whereas the sun position is to the left, and the local times are indicated. No measurements were collected within $5 R_S$ because in the vast majority of the Cassini passes inside $5 R_S$ the energetic ions (keV energy range) are effectively absorbed due to charge exchange with Saturn's neutral cloud, sourced from Enceladus.

sheet presents a northward (southward) displacement before (after) solstice, as a result of the geometry of the solar wind flow with respect to the planet's magnetospheric tilt, creating its characteristic *bow-shape* (N-S asymmetry), previously explained by Arridge et al. (2008) and confirmed by Carbary and Mitchell (2016) using Energetic Neutral Atom (ENA) measurements from MIMI/INCA.

Here we employ all available measurements for the dayside and nightside magnetosphere, and do not limit the selection of data to orbits with the above characteristics, in order to map our ion distributions to the equatorial plane (described in sections 3, 4, and 5). Assuming a centered dipole planetary magnetic field, the dipole- L parameter is defined as $L = R/\cos^2\lambda$, where R is the radial distance in R_S ($1 R_S = 60,268$ km) and λ is the magnetic latitude. However, starting from equatorial distances of $5 R_S$, Saturn's magnetospheric field deviates from that of a simple dipole. If these deviations, which maximize beyond $10\text{--}12 R_S$ (Khurana et al., 2009), are not considered, they may cause systematic errors in the mapping of the ion parameters, especially if the mapping is done from high latitudes to the magnetic equator, imposing a lower bound on their radial location.

Consequently, the use of a more realistic magnetic field model, that involves stretched magnetic topologies, is essential to be able to correctly map the ion distributions to the equatorial plane, reduce these systematic errors, and interpret our results. Here we employ the Khurana et al. (2006) model that is frequently used in the literature and provides such a realistic magnetic field. The model is based on Cassini/MAG measurements (Dougherty et al., 2004) to map high latitude data to the equatorial plane and was first introduced in Khurana (1997) for Jupiter including an internal field plus current sheet perturbation, but the update for Saturn (used here) includes—in addition—magnetopause and tail fields. Our primary purpose for using this model (among other, equally effective models; e.g., Achilleos et al., 2010) is to reduce as much as possible the systematic error induced by mapping high latitude measurements to the magnetic equator through a dipole. In this way, we do not have to exclude a large number of measurements from our statistics, as done in other cases, where latitudinal filters are applied.

3. Energetic Ion Kappa Parameters

Figure 1 illustrates sampled energetic ion H⁺ (30 min accumulation time) and O⁺ (1 hr accumulation time) energy spectra from Saturn's magnetosphere ($5 < L < 20$) using CHEMS, LEMMS, and INCA measurements. The flattening/relative peak of the energy spectra that occurs in the ~30–150 keV energy range for both species, together with the high-energy tail (>200–300 keV), which differs from a Maxwellian distribution, is characteristic of a nonthermal spectral shape/behavior and enables the use of a κ -distribution function (Dialynas et al., 2009). Further, employing a Maxwellian distribution would result in a significant underestimation of the particle temperature (Nicolaou & Livadiotis, 2016).

$$j = CE[E + T_{\kappa}(1 + \kappa)]^{-(1+\kappa)}. \quad (1)$$

The functional form of the κ -distribution function shown in equation (1), with j corresponding to the measured particle differential intensities ($(cm^2 \cdot s \cdot sr \cdot keV)^{-1}$), was adopted from Mauk et al. (2004). Here we do not include the additional term that captures possible high-energy softening breaks (denominator of equation (1) in Mauk et al., 2004), a situation that applies in the energetic ion spectra in the Jovian magnetosphere, but not in Saturn's magnetosphere (see also Dialynas et al., 2009), at least for the energy range considered here. In equation (1), as will be explained in what follows, κ is the distribution's tail exponent, T_{κ} is an effective temperature, E is the particle kinetic energy, and C is a constant.

In this case, E is the measured particle energy expressed in keV, assuming that all measurements are made in the reference frame of the plasma flow. In principle, the determination of E in equation (1) relies on the necessity to have measurements in a variety of look directions relative to the convection frame (Dialynas et al., 2017). Corrections of E for possible flow anisotropies are very minor, however, as our measurements are performed over various look directions that involve both spacecraft *spin* and *stare* periods, and together with the relatively conservative averaging of the data (>30 min accumulation times) we obtain a good sampling with respect to the flow direction. Notably, apart from the good spatial coverage, MIMI provides measurements that include high-energy resolution, consistent with Poissonian statistics ($\frac{\Delta E}{E} \sim E^{-0.5}$), allowing the reconstruction of the energy spectra in the plasma rest frame with very low relative percentage errors (see Figure 1).

The T_{κ} parameter in equation (1) scales the actual temperature (T) of the system after employing the derived κ -index (Dialynas et al., 2017; Livadiotis & McComas, 2009):

$$T_{\kappa} = T \frac{\kappa - 3/2}{\kappa + 1}. \quad (2)$$

We should note that the above scaling of T with κ and T_{κ} does not imply that the temperature (T) depends on the κ -index, a misinterpretation that might be extracted from equation (2). The temperature is a fundamental thermodynamical parameter itself that does not depend on any other thermodynamic parameter (Livadiotis, 2017). Thus, any relation of the temperature and the κ -index (such as equation (2) here and/or others that are not shown here) may be coincidental and/or depend on specific plasma conditions. Here equation (2) connects these parameters because of the way that the modified κ -distribution was defined compared to the functional form introduced by Vasyliunas (1968; see Livadiotis and McComas, 2009, for detailed algebraic calculations on this point). This issue will be highlighted in section 5.3 where a simulation of the temperature in relation to the pressure and density derived from these data is performed.

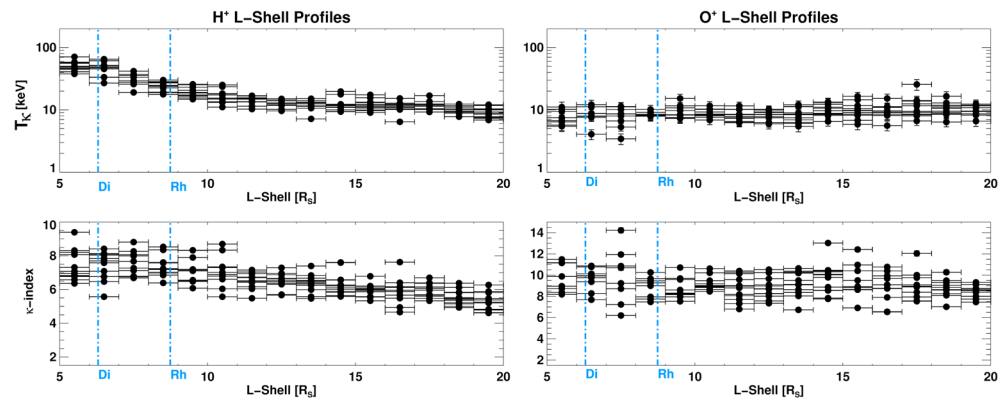


Figure 3. Proton (top left) and oxygen ion (top right) T_{κ} profile (in keV) as a function of L-shell ($5 < L < 20$) that resulted from direct fits with κ -distributions in the >20 keV energy range. (bottom left) The κ index of H^+ and (bottom right) O^+ as a function of L-shell ($5 < L < 20$). Although the κ -index profiles are highly variable for both species, protons show a slight trend with L-shell, with higher κ s in the innermost parts of the magnetosphere, whereas O^+ does not show any specific trend with L-shell. Due to the very low relative percentage errors in the κ -distributions fits (see Figure 1) and the accumulation of a large number of data at each L-shell and LT bin (explained in section 3), the uncertainties associated with these parameters are comparable or smaller than the data points. The horizontal uncertainties correspond to the $1 R_S$ binning in L-shell.

Our aim is to obtain a semiempirical, analytic representation of the energetic ion moments at Saturn. Therefore, by contrast to the Dialynas et al. (2009) technique, here we fit only the >20 keV energetic ion measurements instead of employing an additional power law in energy to capture the turnup in intensities over the <20 keV ion measurements that we have previously identified as the high-energy tail of a cold ion population (Young et al., 2005), that is, a first, *low energy* κ -distribution (Dialynas et al., 2009). Ideally, the use of low energy ion measurements combined with the MIMI data, as was performed in Schippers et al. (2008) for <30 keV electrons, further employing a superposition of κ -distributions would result in the full characterization of the plasma environment in Saturn's magnetosphere. However, such an analysis goes beyond the scope of the present study.

The resulting fit parameters, shown in Figure 2, were binned into a grid with dimensions of $1 R_S$ in L-shell and 30° in LT (2 hr) and were averaged at each bin to produce these equatorial distributions of T_{κ} and κ -index. The $H^+ T_{\kappa}$, κ , and T (equation (2)) equatorial distributions show slight day-night as well as dusk-dawn asymmetries, consistent with similar asymmetries shown in the ring current energetic ion fluxes presented in Dialynas et al. (2013) and other studies involving different charged energetic particle, ENA, plasma, and field measurements and simulations (e.g., Allen et al., 2018; Carbary et al., 2008; Jia et al., 2012; Kollmann et al., 2011; Thomsen et al., 2012; Sergis et al., 2017). As also illustrated in Figure 2, the $H^+ T_{\kappa}$ and T gradually increase in the inner parts of the magnetosphere, reaching >30 keV, which implies that protons get heated while moving toward stronger magnetic fields closer to the planet. By analogy, the κ -values of protons increase toward the planet, implying that as the distributions become hotter, they also become more Maxwellian ($\kappa \rightarrow \infty$).

As we already noted in the section 1, the κ -index of energetic particles controls how much energy flux is out of equilibrium in the distribution's tail (i.e., not part of a Maxwellian). Therefore, it can be related to the free energy in a specific system, thus characterizing the system's state alone, independently of the existence of a possible reservoir interacting with that system. A metric that describes how close a given system is to equilibrium can be achieved through the κ -value: $M_q = 4(q - 1)/(q + 1)$, where $q = 1 + 1/\kappa$ (Livadiotis & McComas, 2010). The ion distributions at Saturn get closer to equilibrium ($q \rightarrow 1$, $M_q \rightarrow 0$) in the inner magnetosphere, where the κ indices are generally higher. However, given the relatively limited range of κ -indices between the inner and outer parts of the magnetosphere, we infer that the energetic ions are generally away from equilibrium. For example, at $L \sim 20 R_S$, where $\kappa \sim 4$ (for H^+), the thermodynamic distance of H^+ from equilibrium is $q \sim 1.25$ (the furthest possible stationary state from equilibrium, where $M_q \sim 44\%$), whereas at $L \sim 6$, where $\kappa \sim 8$ (for H^+), $q \sim 1.13$ ($M_q \sim 23.5\%$). Nevertheless, due to the statistically significant decrease of κ -index (for H^+) outward, we infer that protons move (thermodynamically) away from equilibrium, a situation that does not seem to apply for the singly ionized oxygen, where the κ remains almost constant throughout the $5 < L < 20$ region ($\kappa \sim 8-10$, $q \sim 1.13-1.1$, $M_q \sim 23.5-19\%$).

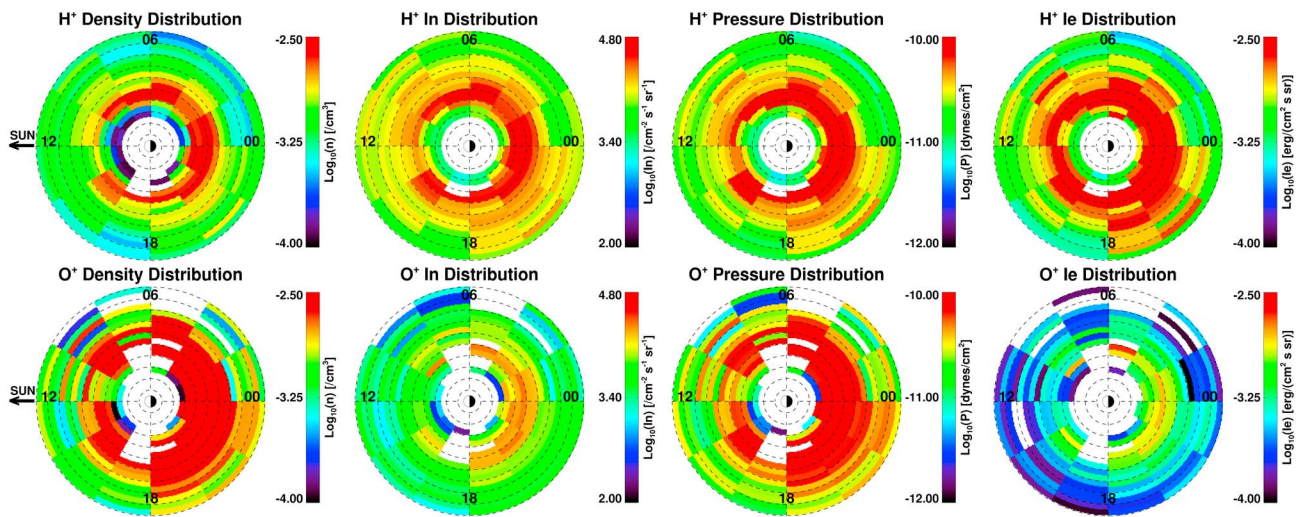


Figure 4. (top) Equatorial distributions of integral energetic H⁺ moments (>20 keV), in the same format as in Figure 2 (see legends for details). (bottom) The same integral moments for O⁺.

In principle, κ -distributions are thermodynamically stable, independently of the value of the κ -index, whereas their transition to different thermodynamic states that include higher or lower κ values can occur via several different mechanisms (c.f. Livadiotis, 2017). Higher κ -index values may imply *older* distributions, in the sense that they may have undergone more velocity space diffusion (among other mechanisms), whereas spectra with high-energy tails that include relatively small κ -indices may imply newly formed distributions. This is not inconsistent with the fact that the outer parts of the Saturnian magnetosphere are dominated by a series of (quasi-)periodic injections of energetic ions (e.g., Mitchell et al., 2009), that are subsequently subject to radial propagation (Paranicas et al., 2016; Rymer et al., 2009), the corotation electric field that dominates the transport of particles even up to 100 keV (Brandt et al., 2008), and charge-exchange decay (Dialynas et al., 2013).

The H⁺ T_{κ} increase toward Saturn (toward increasing field strength) in the inner to middle magnetosphere (<20 R_S ; see Figure 3) implies energization by conservation of the first adiabatic invariant (magnetic moment; $\mu = W_{\perp}/B$, $W_{\perp} = \frac{1}{2}mv^2\sin^2(a)$, where a is the particle's pitch angle with respect to the magnetic field B). Inward transport of particles has been also observed in the electron data using the LEMMS sensor by Paranicas et al. (2010), showing that the energization process of injections is consistent with the conservation of the two adiabatic invariants (bounce and μ) for the case of energetic electrons. We note that this characteristic behavior of H⁺ in the middle to outer magnetosphere (>15 R_S) could also be interpreted as adiabatic energy loss with outward transport, since anisotropy studies (Kane et al., 2014) showed that radial transport is primarily outward in the outer magnetosphere, out beyond ~ 20 to $\sim 50 R_S$. Interestingly, plasma ions from the Cassini/CAPS detector (Thomsen et al., 2014) showed a radial mass outflow of ~ 34 kg/s (and less, but existing, inflow), located mainly in the dusk to midnight sector (18:00 to 03:00 in local time), in the same radial range as in the Kane et al. (2014) study. Although our measurements correspond to energetic particles and are limited to <20 R_S , this compares well with the asymmetry shown in both the H⁺ T_{κ} and κ -index distributions in Figure 3 (and in the statistical energetic ion moments shown in the next section), although the reason is unclear to us at this point.

By contrast, the O⁺ parameters do not exhibit similar characteristics and both the O⁺ κ -index and T_{κ} remain almost constant throughout the magnetosphere ($T_{\kappa} \sim 10$ – 20 keV, $\kappa \sim 8$ – 10), with a possible dusk-dawn asymmetry which may be the effect of limited statistics of O⁺ over the dawn sector. The lack of a trend of either T_{κ} and κ -index as a function of L-shell implies that O⁺ may be heated locally at each L-shell as previously shown in Dialynas et al. (2009).

Although mapping the H⁺ and O⁺ measurements to the equator may not reflect possible latitude effects for nonequatorially mirroring ions, previous studies (e.g., Dialynas et al., 2009; Krimigis et al., 2007) have shown that plasma sheet temperatures and pressures have minimal latitude dependence. However, magnetic field observations (Khurana et al., 2009) show that in the outermost parts of Saturn's magnetosphere, the ring

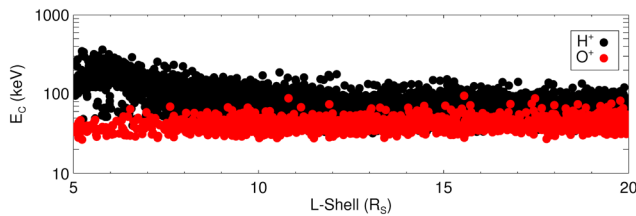


Figure 5. (a) Characteristic Energy, $E_C (=I_E/I_n)$ as a function of L-shell for both >20 keV H^+ and O^+ particles, using all available energetic ion spectra in Saturn's magnetosphere over the 2004–2017 time period.

current and the current sheet add to the planetary dipole magnetic field, resulting in a stretched magnetic field configuration, that is, the $>12 R_S$ region is where the magnetic field lines deviate significantly from the dipole approximation at Saturn. This is a prime indicator of ion acceleration in magnetic field reconfigurations during the relaxation phase of the magnetic field lines, similar to what happens at Earth (e.g., Delcourt, 2002) and/or due to multiple injection events that occur in Saturn's magnetosphere, in either the innermost regions (e.g., Azari et al., 2018) and/or the middle to outer parts (e.g., Mitchell et al., 2009).

4. Energetic Ion Integral Moments

The velocity distribution function (κ -distribution in our case) provides a *microscopic* description of statistical information on the energetic charged particles that we study here, but a very important use of it is the determination of the *macroscopic* parameters that are fundamentally important for studying the transport and properties of energetic plasma inside the magnetosphere. The modeled expressions of the energetic ion energy spectra (modeled κ -distributions) are incorporated in the set of the velocity moment equations explained in Mauk et al. (2004), to obtain the four integral particle moments (shown in Figure 4), namely, density (n), Integral number intensity (I_n), Pressure (P), and Integral energy intensity (I_E), via analytic integration.

As expected, the H^+ and O^+ partial pressures are comparable throughout Saturn's magnetosphere, that is, $\sim 50\%$ of the $>8 R_S$ partial ion partial pressure comes from O^+ , consistent with earlier studies that employed MIMI measurements to calculate the partial H^+ and O^+ pressures using different techniques that involve direct numerical integrations (e.g., Sergis et al., 2007). Of special interest is the fact that O^+ particles dominate the >20 keV density over most radial distances and local times. This is also a result shown in the recent study of Allen et al. (2018), where the equatorial distributions of W^+ and H^+ revealed higher densities for the former species. However, H^+ dominates the energetic ion integral number and energy intensity at all radial distances ($L > 5$) and local times by at least one order of magnitude (as in the Allen et al., 2018, study as well).

The characteristic energy (E_C) profiles of >20 keV H^+ and O^+ particles (Figure 5), calculated from the ratio between the energetic ion integral energy intensity and the integral number ($E_C = I_E/I_n$) that corresponds to the peak in the differential flux (characteristic particle speed), show comparable dependence for $>8-12 R_S$. However, the characteristic energy of O^+ particles remains nearly constant throughout $5 < L < 20$, whereas the characteristic energy of H^+ is increasing toward Saturn. The increased E_C values for H^+ , especially inside of $8-12 R_S$, can be either due to a thermalization of the H^+ distributions (consistent also with the calculated κ -index) and the *temperature* increase closer to the planet due to acceleration of particles toward stronger magnetic fields, or an effect of charge exchange of ions with the ambient neutral distributions that become increasingly important in the inner magnetosphere, closer to the vicinity of Enceladus, or to a combination of both these effects.

The O^+ lifetimes inside the magnetosphere (Dialynas et al., 2009) are slightly longer than H^+ lifetimes over the $<20-40$ keV, but the $>20-40$ keV H^+ lifetimes are much greater. Therefore, as the O^+ density increases toward the planet and yet E_C remains constant, it implies that little energy is gained by adiabatic heating as O^+ ions move toward the planet to stronger magnetic fields. By contrast, the increasing E_C and density of H^+ together with relatively long H^+ lifetimes (H^+ particles survive much more efficiently than O^+ inside Saturn's magnetosphere) imply that proton energization is fairly consistent with adiabatic heating. Although the charge-exchange mechanism alone may not resolve all details concerning the differences between the energetic H^+ and O^+ spectra, as inferred by the very simplified model in Kollmann et al. (2015, see Appendix A) we note that if a realistic neutral gas distribution is factored in (e.g., Dialynas et al., 2013), one would obtain a set of realistic energetic ion lifetimes, providing an invaluable input to study the energization of charged particles in the Saturnian system. However, this task goes beyond the scope of the present study.

Of special interest is the sudden decreasing trend of the H^+E_C inside of $\sim 6 R_S$, that is, closest to Enceladus, which suggests that the losses in this region, reflected in a corresponding density decrease, are indicative of dramatic increase of the charge-exchange loss rate. This is consistent with the Paranicas et al. (2008) observations, who reported that the energetic ions are effectively absorbed inside $\sim 5 R_S$ to $\sim 6 R_S$, so that this region is almost void of more energetic protons or singly ionized oxygen. Clearly, Saturn's neutral cloud plays a key

role in determining the shapes of the ion spectra, presenting a significant loss term of the >20 keV ions. We will return to this point in section 7.

5. Simulations

There are numerous models developed over the Cassini era to describe the pressure distribution and particle flow properties in the Saturnian system (e.g., Achilleos et al., 2010; Brandt et al., 2010; Jia et al., 2012). Here we do not aim to study the driving mechanism(s) behind the ring current formation, rather than provide a simple model as a stepping stone to obtain physically meaningful results concerning the adiabatic versus nonadiabatic properties of charged particles in the magnetosphere. Thus, in order to simulate the ion (H^+ and O^+) equatorial partial pressure distributions as a function of both L-shell and local time, it is necessary to employ a well-constrained, parameterized ion model that can, in addition, manage a large number of measurements. We use the Roelof and Skinner (2000) semiempirical model (also used in other studies, e.g., Brandt et al., 2010, 2012; Dialynas et al., 2013), suitably modified to simulate the partial pressure rather than the energetic ion flux.

The ion pressure in equation (3) is defined in the equatorial plane with separable functions in azimuthal angle (note that local time = $[(\phi+180)\text{mod}360]/15$) and L-shell. Although the model provides the framework for a separable function for the ion pitch angle distribution, since we employ mission averaged measurements, we have assumed isotropic pitch angle distributions for both species in the present study. In mathematical formalism, the model is written as follows:

$$P = P_0 \exp(-f_\phi(\phi) - f_L(L)). \quad (3)$$

The exponential form of equation (3) assures that the partial pressure is positive definite, as it must be physically, and can describe the observed variable ion pressures throughout the magnetosphere, where linear expressions may fail to perform.

For the L-dependence, the pressure distributions are written as

$$f_L = \begin{cases} \frac{(L-L_1)^2}{2\delta L_1^2} & L < L_{11} \\ \frac{L-L_{11}}{L_0} + \frac{1}{2} \left(\frac{\delta L_1}{L_0} \right)^2 & L_{11} \leq L \leq L_{22} \\ \frac{(L-L_2)^2}{2\delta L_2^2} + \frac{L_2-L_1}{L_0} + \frac{1}{2} \left(\frac{\delta L_2}{L_0} \right)^2 - \frac{1}{2} \left(\frac{\delta L_1}{L_0} \right)^2 & L > L_{22} \end{cases} \quad (4)$$

where the L-shell dependence in equation (4) forms a Gaussian in the inner regions of the magnetosphere that change smoothly to an exponential decay function (at $L = L_{11}$, $L_{11} = L_1 + \frac{\delta L_1^2}{L_0}$), followed by a second Gaussian in the outer regions of the magnetosphere (at $L = L_{22}$, $L_{22} = L_2 + \frac{\delta L_2^2}{L_0}$). The parameters L_1 and L_2 denote the L-shell values where the first and the second Gaussian functions peak, while δL_1 and δL_2 represent the Half Width at Half Maximum of the two Gaussians, respectively. The slope of the exponential function in the region $L_{11} \leq L \leq L_{22}$ is controlled by the parameter L_0 .

For the azimuthal dependence, the model uses a two harmonic expansion that allows us to modulate the ion pressure in Local Time so that we can obtain a region of maximum pressure, that is, a day to night asymmetry (controlled by parameter ϕ_1) and at the same time, using the second term, a dusk to dawn asymmetry (controlled by parameter ϕ_2).

$$f_\phi = k_1 [1 - \cos(\phi - \phi_1)] + k_2 [1 - \cos 2(\phi - \phi_2)]. \quad (5)$$

The above functions depicted in equations (3)–(5) are used to perform 2-D fits to the energetic ion equatorial distributions shown in Figure 4 (specifically the P , n , and T , as will be shown in the upcoming sections). Note that the user should be careful to differentiate these spatial distributions as described in equations (3)–(5) from the κ -distributions in energy. The goodness of the fit is determined by the normalized χ^2 parameter (Press et al., 1992), where assuming that s_i represent the set of N simulated pixels ($i = 1 \dots N$), a_i is the set of observed pixel values and σ_i is each pixel's standard deviation, then

$$\chi^2 = \frac{1}{N} \sum_{i=1}^N \frac{(s_i - a_i)^2}{\sigma_i^2}. \quad (6)$$

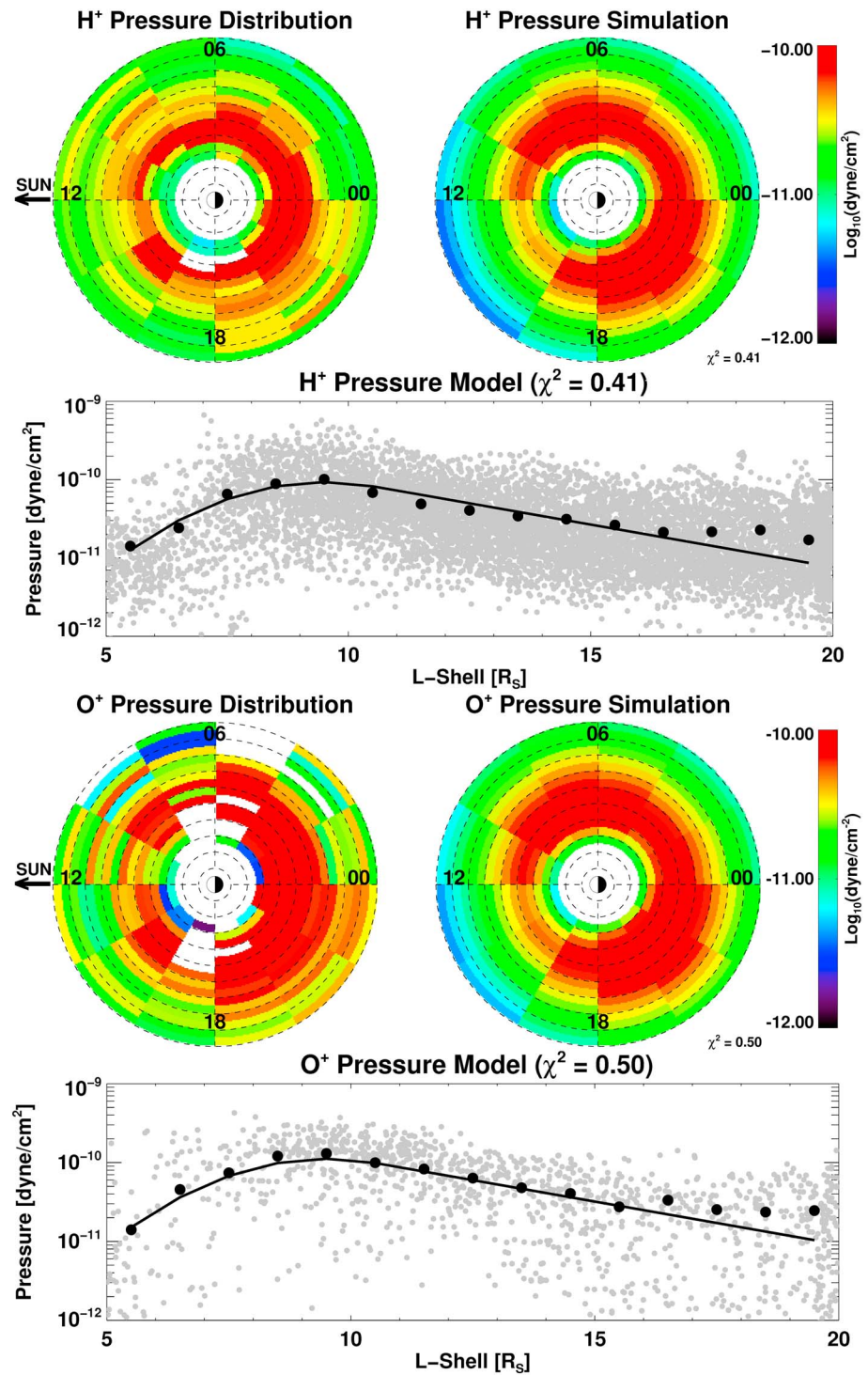


Figure 6. (top panel) H⁺ partial pressure shown in Figure 3 together with the simulated partial pressure as a function of local time and L-shell that resulted after a 2-D fit of the Roelof and Skinner (2000) semiempirical model to the data ($\chi^2 = 0.41$). (Line plot) Black points represent an average of the calculated partial pressure profiles (gray points) at each local time sector, as a function of L-shell. The line represents the Roelof and Skinner (2000) fit to these data. (bottom panel) The same for O⁺.

Since equation (6) is normalized by the number of pixels that are employed in the fit (M), and the numerator is dominated by Poisson fluctuations, ideally χ^2 would converge to unity for a perfect fit. However, as the model does not include an instrument background we accept solutions for which $\chi^2 < 1$. We note that although the use of the reduced χ^2 parameter, that is, normalizing equation (6) by the number of pixels minus the number of fitted parameters, is generally more efficient/precise than the normalized χ^2 function, due to the large number of measurements that we simulate, the two methods are not expected to produce different results (in the accuracy afforded by our measurements). Therefore, we have selected to remain fully consistent with the Roelof and Skinner (2000) application that includes the use of equation (6).

5.1. Energetic Ion Partial Pressure

The >20 keV H^+ and O^+ partial pressure equatorial distributions in Figure 6 are consistent with the corresponding equatorial distributions shown recently in Sergis et al. (2017). Both species are consistent with an asymmetric ring current distribution, exhibiting a day-night and a dusk-dawn asymmetry. The nightside magnetosphere presents—on average—an extended region of maximum partial pressure that spans over ~ 6 – $14 R_S$ in L-shell and $\sim 18:00$ to $6:00$ on the night sector, whereas the peak of these partial pressure distributions seem to lie toward the post-dusk sector. We note that these equatorial distributions describe an average situation which refers to ~ 12 years of observations and therefore do not capture the dynamics of a rotating ring current explained earlier in the literature.

The application of the Roelof and Skinner (2000) model, as described in the previous section, is shown in Figure 6 for both H^+ and O^+ . The simulated H^+ and O^+ distributions show a clear day-night asymmetry (centered at local midnight in our simulation, 180° from local noon, while $k_1 = 0.4$) with a peak pressure of $P_0 \sim 2 \times 10^{-10}$ dynes/cm² for H^+ , that occurs at $L_1 \sim 9.5 R_S$ ($\delta L_1 \sim 2 R_S$), while the O^+ the peak pressure is slightly higher, $\sim 2.2 \times 10^{-10}$ dynes/cm², but occurs at the same radial distance ($L_1 \sim 9.5 R_S$) and retains the same Gaussian spread ($\delta L_1 \sim 2 R_S$, $\delta L_2 \sim 6 R_S$), $\sim 35^\circ$ premidnight for both species (creating the apparent dusk-dawn asymmetry, while $k_2 = 0.45$). This rotation is consistent with recent studies that measured energetic ion injections that occur preferably in the night sectors of the magnetosphere (e.g., Azari et al., 2018). The minor peaks for H^+ and O^+ occur at $L_2 \sim 15 R_S$, while both species partial pressures drop with the same slope ($L_0 \sim 4 R_S$) between the two Gaussian peaks. Note that our simulation includes uncertainties associated with the aforementioned L-values and angles due to 30° and $1 R_S$ binning in LT and L-shell, respectively (see Section 3).

The scattered data plots in Figure 6 (gray data points) represent the calculated partial pressure profiles, directly from the κ -distribution fits. The success of the Roelof and Skinner (2000) fit is apparent for both species, that is, the model (black lines) as a function of L-shell provides a good match to the average partial pressures as a function of L-shell (black points) throughout the $5 < L < 17$ – 18 regions. However, the data suggest a pressure increase in the outer (>17 – $18 R_S$) parts of the magnetosphere (a factor of ~ 2 for both H^+ and O^+), which may be the result of the multiple energetic ion injections that occur in this region, adding pressure to the system, that our model is not capable of capturing (this effect is also shown in the partial density profiles discussed in section 5.2). We infer that the energetic ion bundles in the $12 < L < 20$, and especially beyond ~ 17 – $18 R_S$ (where charge exchange is very limited compared to the inner magnetospheric regions), that—possibly—result from rotating energetic particle blobs shown in previous studies (e.g., Carbary et al., 2008; Mitchell et al., 2009), produce durable signatures (enhancements) in the H^+ and O^+ pressure and density. We will return to this point in section 7.

Local time asymmetries have also been observed in energetic particle Phase Space Densities, Electron temperatures (T_{e^-}), and plasma flows (Thomsen et al., 2012; Wilson et al., 2013) and reproduced in magnetohydrodynamic simulations (Jia & Kivelson, 2016). They are thought to result from a convective E-field (Andriopoulou et al., 2014) with a noon-midnight orientation, resulting (partly) from adiabatic radial transport. In that sense, it is puzzling why O^+ in our analysis indicates that it behaves nonadiabatically. However, the role of charge exchange of O^+ particles with Saturn's neutral gas distributions discussed in section 4, resulting in relatively small O^+ lifetimes, (partly) resolves this conundrum.

An additional puzzle concerns the local time asymmetry between the peaks of the energetic particle pressure and density (see section 5.2) shown here (peaks lie in the dusk-midnight sector, consistent with the results in Sergis et al., 2017) and the noon-midnight preferred orientation in Andriopoulou et al. (2014). We note, however, that all the ion distributions shown in this study include a secondary peak that lies in the post-dawn sector ($\sim 20^\circ$), consistent with the aforementioned noon-midnight electric field. A detailed description on the

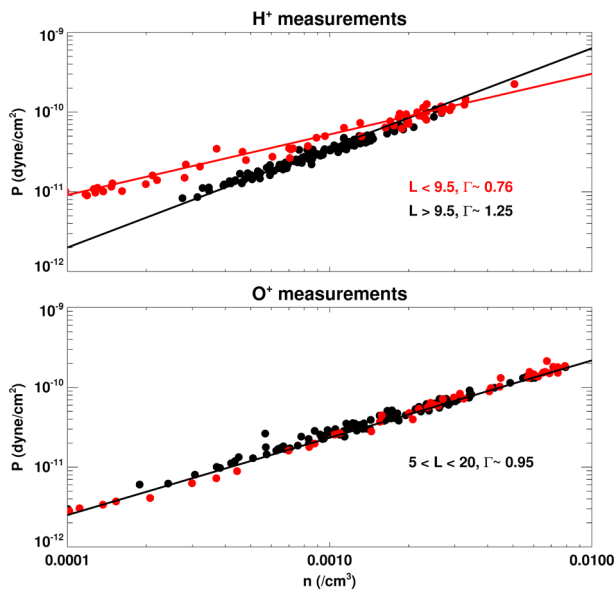


Figure 7. Distributions of the partial energetic (top) H^+ and (bottom) O^+ pressure and density from the equatorial distributions shown in Figure 4. Red points correspond to (P, n) pairs in the $5 < L < 9.5$ region and black points in the $9.5 < L < 20$ region as explained in the legend.

complications between the theoretical expectations and simulations concerning the nature and source of an asymmetric electric field can be found in Jia and Kivelson (2016).

Here we should mention that (a) our measurements correspond to ~ 12 years of in situ observations, which possibly indicates that some of the rotational energetic particle flow properties are averaged out, especially since the pressure calculation performed here incorporates a wide range of different energy particles, whereas the noon-midnight electric field will produce different effects as a function of energy; (b) the simulations shown in Jia et al. (2012) present an azimuthal current distribution that remains fixed over a broad region in local time on the night sectors, $\sim 18:00$ to $\sim 06:00$ hr, over a planetary rotation which is consistent with our ion distributions. A slight radial displacement of the peak in the ring current distribution between our results ($\sim 9.5 R_S$) and the Jia et al. (2012) simulations ($\sim 10-15 R_S$) is possibly attributed to “[...] the underestimation of the contribution of the hot plasma pressure for $R > 10 R_S$ that largely controls the azimuthal current density” as noted by Sergis et al. (2017).

5.2. Energetic Ion Density

Although the energetic ion (> 20 keV) partial densities are some orders of magnitude lower than the corresponding densities which characterize the thermal plasma (e.g., Wilson et al., 2017), the derivation of the energetic ion partial density provides an invaluable input to the determination of the equation of state. This is very frequently used in magnetohydrodynamic

descriptions of plasma convection in planetary magnetospheres and can serve as a proxy for the local entropy (e.g., $S = T/n^{\Gamma-1}$, sometimes called *specific entropy*), pointing also to the transport of plasma inside the magnetosphere (e.g., Wing & Johnson, 2010, and references therein). In the generalized view of the equation of state, the pressure relates to the ion density by $P = Cn^\Gamma$.

In this expression, Γ is the polytropic index (defined as the ratio between the specific heat at constant pressure and constant volume, c_p/c_v), that for an adiabatic process in an ideal gas with f degrees of freedom, $\Gamma = (f+2)/f$, that is, $5/3$ if we assume that the plasma sheet distributions are isotropic ($f = 3$). The polytropic index is one of the fundamental physical parameters of plasmas and provides useful information on the internal processes that a plasma undergoes: In principle, an isobaric plasma process would be represented by $\Gamma = 0$ (where $P = \text{const.}$) while an isothermal process by $\Gamma = 1$ (where the $T = \text{const.}$). Despite its physical context, Γ cannot be measured directly in space and an adequate model is required in order to derive its value.

The values of the (P, n) pairs in Figure 7 provide a first indication concerning the thermodynamical processes that are taking place inside the $5 < L < 20$ region for both H^+ and O^+ . Clearly, the energetic H^+ (P, n) distributions are separated in two different parts: (a) outside $9.5 R_S$ (black points in Figure 7) where the polytropic index is ~ 1.25 implying a subadiabatic process and (b) inside $9.5 R_S$ (red points in Figure 7) where the polytropic index is ~ 0.76 implying a sub-isothermal process. The situation concerning the O^+ is different and the (P, n) pairs form a single distribution throughout the $5 < L < 20$ region with a polytropic index that is ~ 0.95 implying a quasi-isothermal behavior.

Although the (P, n) distributions in Figure 7 provide a useful estimation of the polytropic index, all the spatial information (radial distance and local time) are collapsed into a single dimension. However, having the energetic ion partial pressure distribution modeled (see section 5.1), we can search for suitable Γ in order to match the simulated H^+ and O^+ densities with the calculated ones (from the κ -distribution fits), starting from the ones extracted from Figure 7.

Our model, concerning the O^+ densities, shown in Figure 8 (bottom panel), includes a single polytropic index extracted from Figure 7, indicating that the O^+ particles behave quasi-isothermally for all regions $5 < L < 20$ and all local times, with $\Gamma = 0.95$. We note that we were able to obtain almost equally good solutions using Γ ranging from ~ 0.85 to ~ 1 . As was already mentioned earlier in this section, the situation for H^+ is more complicated than O^+ (see Figure 7): H^+ behaves sub-isothermally ($\Gamma = 0.76$) for all local times with $L < 9.5$ but exhibits a subadiabatic behavior at all local times where $L > 9.5$, that is, $\Gamma = 1.25$. Again, to obtain a 2-D rep-

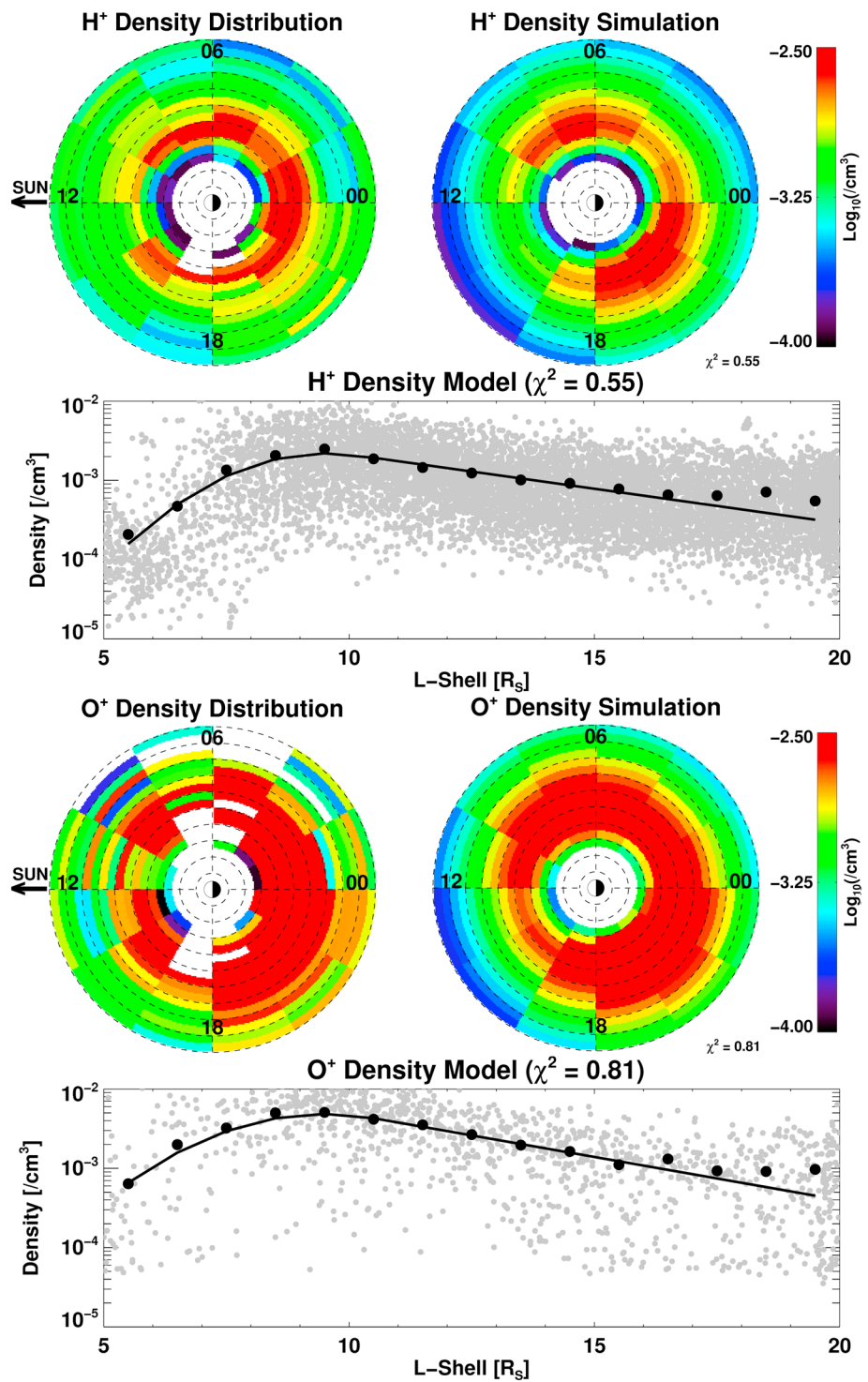


Figure 8. (top panel) H⁺ partial density shown in Figure 3 together with the simulated partial density as a function of local time and L-shell that resulted after a 2-D fit of $P = Cn^{\Gamma}$ to the partial density data. (Line plot) Black points represent an average of the calculated partial density (gray points) at each local time sector, as a function of L-Shell. The line represents our simulation. (bottom panel) The same for O⁺.

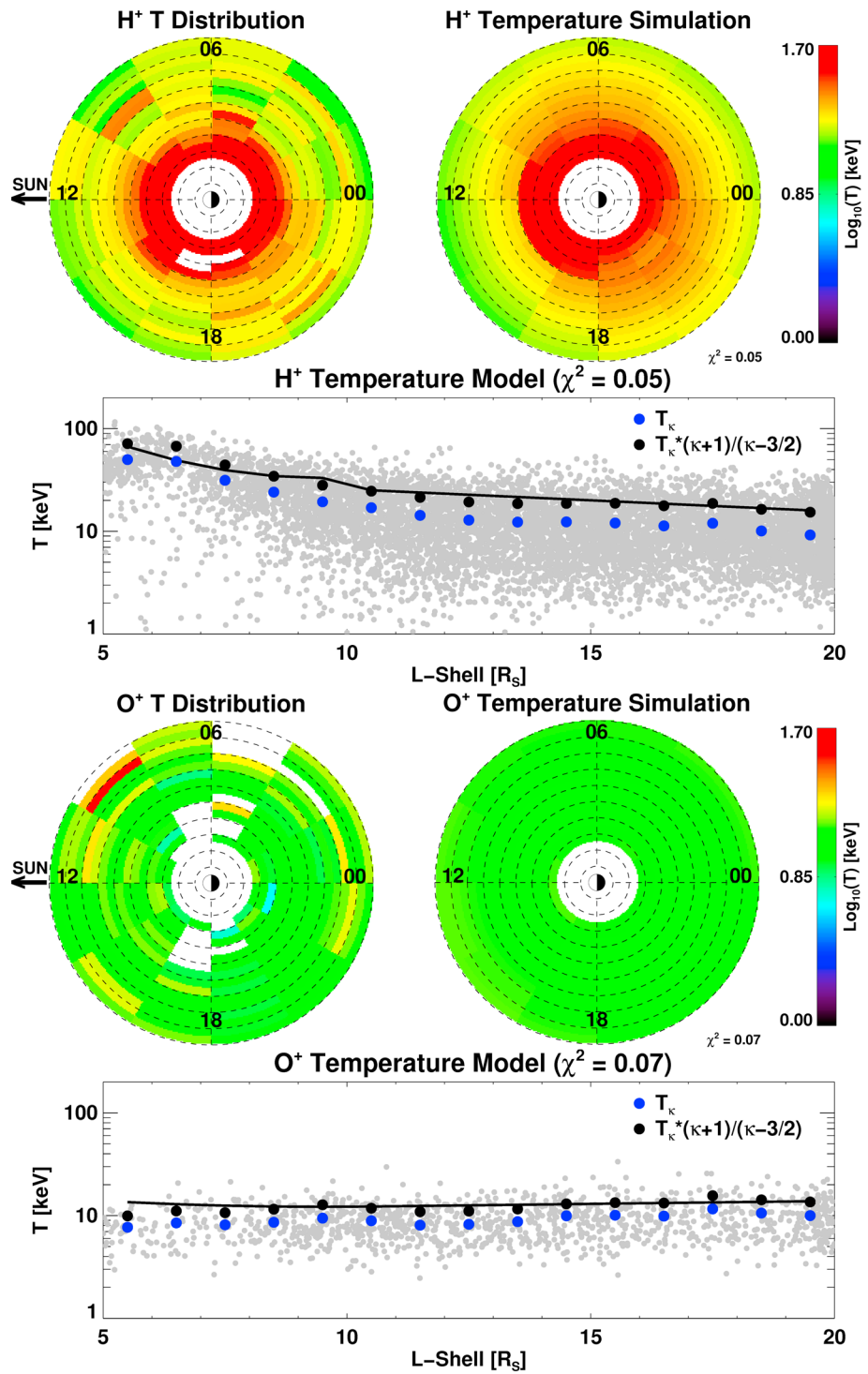


Figure 9. (top panel) Equatorial distribution of H⁺ temperature using equation (2) together with the simulated temperature as a function of local time and L-shell that resulted after a 2-D fit using the simulated P and n parameters (see Figures 6 and 7). (Line plot) Black points represent an average of the calculated temperatures (gray points) at each local time sector, as a function of L-shell. The line represents our simulation. (bottom panel) The same for O⁺.

resentation of the density distribution, we were able to obtain almost equally good solutions with Γ ranging from ~ 1.2 to ~ 1.5 in the $L > 9.5$ region. Notably, in the $L < 9.5$ region the Γ remains pretty stable.

As also shown in the previous section, our fits provide a very good match to the data, except for the $>17-18 R_S$ regions where the model seems to slightly underestimate the densities (on average). Nevertheless, these results are consistent with our previous interpretations (see sections 3 and 4 in this manuscript and Dialynas et al., 2009); H^+ is heated quasi-adiabatically, whereas O^+ is heated locally at each L-shell, subject to nonadiabatic acceleration and charge exchange. While β is significantly >1 beyond $8-10 R_S$ (Sergis et al., 2017), adding the magnetic field pressure to the simulations is not expected to affect the calculation of Γ significantly. Our results are consistent with the corresponding analyses of electron data (Arridge et al., 2009), where $\Gamma \sim 1$, with many cases approaching adiabatic behavior ($\Gamma > 1$ and $< 5/3$).

5.3. Temperature of Energetic Ions

Although the use of a κ -distribution function in order to describe our energetic ion spectra implies that the energetic ions are not found in a classical thermodynamic equilibrium state inside the magnetosphere, the ideal gas state equation $P = nk_B T$ (k_B =Boltzmann's constant) still holds for any nonequilibrium stationary state (Livadiotis & McComas, 2012). Consequently, through this equation, we can also obtain an analytic representation of the temperature of energetic ions ($T = T_\kappa(\kappa + 1)/(\kappa - 3/2)$) after applying the calculated polytropic index for either H^+ or O^+ . In other words, the temperature can also be described by the polytropic law, that is, $n \sim T^{\frac{1}{\Gamma-1}}$.

The resulting fits are shown in Figure 9. As expected, using the simulated density and pressure obtained in the previous sections we are able to fit the temperature T and not T_κ (as explained in section 3). However, we note that the best fit for the H^+ temperature (shown in Figure 9) was obtained using a slightly different number for Γ , that is, 0.74 instead of 0.76. On a technical note, the simulation in temperature appears to be very sensitive to the selection of Γ . For example:

1. For the O^+ distributions, using Γ values bellow 0.85 we may obtain a good fit to most parts of the magnetosphere, but the simulation creates a slight turnup in innermost regions, that is, $< \sim 8 R_S$, and fails to remain almost constant as the measurements imply.
2. For the $>9.5 R_S$ H^+ distributions, using Γ values bellow 1.2, the temperature gradually flattens and fails to capture the increasing trend shown in the measurements.

Notably, due to the low χ^2 parameters for both fits (approaching zero), we infer that our fits are subject to large standard deviations, as explained in section 5.

Nevertheless, the simulations in temperature verify that the H^+ follow a rough quasi-adiabatic law (being subadiabatic) in most parts of the Saturnian magnetosphere ($L > 9.5$), whereas the O^+ temperature remain almost constant throughout the $5 < L < 20$ region and for all local times, following a quasi-isothermal law.

6. Summary and Results

By utilizing all available Cassini/MIMI in situ observations during an extended time period (2004–2016), we have modeled the energetic ion (H^+ and O^+) energy spectra using a κ -distribution form in energy, produced the energetic ion moments equatorial maps for both H^+ and O^+ inside the Saturnian magnetosphere, and simulated the energetic ion partial pressure, density, and temperature using a flexible semiempirical model. Our simulations lead to the extraction of the polytropic index for both H^+ and O^+ , that together with the calculated energetic ion characteristic energies, κ -distribution parameters and lifetimes of ions (due to charge exchange) enables a discussion concerning the energization of ions inside Saturn's magnetosphere. The primary results of this study are summarized as follows:

1. Our measurements include transient injections (and/or aging injections) and at those times protons dominate the energetic ion (>20 keV) integral number and energy intensity at all radial distances ($L > 8$) and local times, while the H^+ and O^+ partial pressures and densities are comparable. However, the O^+ densities in the >20 keV range are slightly higher over most radial distances and local times.
2. The >20 keV energetic ion spectra are consistent with a κ -distribution form in energy and the kappa parameters, together with the calculated energetic ion moments, showed prominent day-night as well as dusk-dawn asymmetries ($\sim 35^\circ$ premidnight) which could be explained by the multiple injections that occur at Saturn, as well as the azimuthal energetic ion flow properties inside the magnetosphere (namely coro-

tation, together with gradient and curvature drifts) in conjunction with charge-exchange decay and/or the noon-midnight electric field as shown elsewhere.

3. The $9.5 < L < 20$ region corresponds to a local equatorial acceleration region, where subadiabatic transport of H^+ , $\Gamma \sim 1.25$ (< 1.67), and quasi-isothermal behavior of O^+ , $\Gamma \sim 0.95$ (< 1), dominate the ion energetics (compared to the contribution of charge exchange with the Saturnian neutral cloud).
4. Nonradiation belt energetic ions are heavily depleted inside the orbit of Rhea ($\sim 8 R_S$), that is, ion lifetimes due to charge exchange decrease significantly with decreasing distance, so that the partial energetic ion pressures and densities drop to minimum inside $\sim 8 R_S$ (see Figures 6 and 8) and the behavior of the energetic ions (both species) appears to be quasi-isothermal ($\Gamma < 1$).
5. Energetic ion bundles in the $9 < L < 20$ (and especially beyond ~ 17 – $18 R_S$), that—possibly—result from rotating energetic particle blobs shown in previous studies, produce durable signatures (enhancements) in the H^+ and O^+ pressure and density.

7. Discussion: Plasma Sheet Thermodynamic State

While all these results are discussed in their corresponding sections of this paper, and compared to relevant studies found in the literature, one of the remaining discussions concerns the implications of these energetic ion properties regarding the stability and thermodynamical state of the plasma sheet itself.

Baumjohann and Paschmann (1989) applied a similar technique as we show here to study the ion properties at Earth's magnetosphere (derived from the equation of state, discussed in section 5.2) and found—on average—a polytropic index of ~ 1.66 during disturbed intervals, implying that during those times the plasma sheet behaves adiabatically, but the quiet plasma sheet behaves as a *poorly insulated vessel*, because $\Gamma \sim 1.39$. Later, Spence and Kivelson (1990), using a 2-D model of adiabatic convection, explored the differences with previous calculations of the polytropic index by Baumjohann and Paschmann (1989) and Huang et al. (1989).

Our results demonstrate that the polytropic index of the energetic ions inside the plasma sheet is ~ 1 and lower than $5/3$ (see sections 5.2 and 5.3 for details), which indicates that the plasma sheet behaves—on average—quasi-isothermally to subadiabatically. This is consistent with the fact that the temperatures for O^+ are almost constant throughout the magnetosphere, whereas the H^+ temperatures follow roughly a quasi-adiabatic law. Earlier analyses from Arridge et al. (2009) using electron (0.5 eV–28 keV) measurements from Cassini showed that the polytropic index is $\Gamma \sim 1.0157 \pm 0.002$, implying that the plasma sheet behaves isothermally on average. However, as noted by the same authors, there are many occasions in their data set where the behavior tends to be adiabatic, as we have also shown here (and/or even isobaric). As far as the electrons are concerned, these authors determined that collisions with H^+ may account for heating the electrons (Rymer et al., 2007), which play the role of an external reservoir that exchanges heat with the system.

The results concerning the energetic ion measurements that we show here add another dimension to this problem. Taking into account the calculated polytropic indices for both electrons (Arridge et al., 2009) and ions shown here (on average $\Gamma \sim 1$ and lower than $5/3$), we arrive at the conclusion that the loss of heat from the plasma sheet is greater than the supply of new energy. New energy can either come from internal sources or from the solar wind. At Saturn, we know that the internal dynamics are much more important than the solar wind input. For example, the rapid rotation at Saturn and the generally weaker solar wind effects result in a large region (up to $L \sim 20$) where the drift due to corotation electric field dominates the transport of ions even up to several 100's of keV (Brandt et al., 2008, 2010), whereas recent modeling suggests that the hot plasma dynamics can dominate over solar wind conditions (Pilkington et al., 2015). In principle, multiple injections at Saturn (Mauk et al., 2005; Mitchell et al., 2005, 2009) may account as the drivers of new energy entering the system, but an existing cooling mechanism does not allow the plasma sheet to behave adiabatically, in other words, with no gain or loss of internal energy.

The neutral particles at Saturn, originating from Enceladus (a major source of heavy, mass-loading particles), dominate the ion densities over a very broad magnetospheric region (Vasyliunas, 2008), have a strong influence on the dynamics of the magnetosphere (e.g., Kivelson, 2006, mass density, flow patterns, etc.), and may also act as an effective *cooling mechanism*. The most important consequence of obtaining a $\Gamma < 1.66$ is that the plasma sheet does not have a *ground state*, that is, a stationary state that can be described as being close to (or constantly in some sort of) thermodynamic equilibrium. This was highlighted in section 3 (e.g., through the values of M_q), where we showed that despite the fact that the H^+ distributions get closer to equilibrium as they move toward the planet, they are still away from stationary states that can be characterized as *close to*

local equilibrium, whereas the O^+ retains a stable M_q number throughout the magnetosphere. We, therefore, infer that internal energy is constantly *escaping* by internal processes and new energy entering the system is not enough to balance the losses.

In contrast to electron impact ionization and photoionization, charge exchange does not lead to a net addition of plasma, rather only to a net escape of neutrals (Vasyliunas, 2008). When fast ions interact with the slow neutral particles, the newborn ions that are created by these interactions must be then picked-up by the corotating electric field to be reaccelerated to local corotation speeds. Therefore, these ion-neutral collisions lead to momentum exchanges among ions and neutral particles. Newborn neutrals become more energetic (faster) than the *background* preexisting neutrals. On the other hand, newborn, slow, ions cause a lag on the corotating plasma (Kane et al., 2008; Saur et al., 2004) and, in principle, temperature decrease in the system. Eventually, the charge-exchange decay of ions may result in a continuous plasma sheet cooling.

As we have shown in sections 3 and 4, this situation is most prominent in the case of O^+ throughout the $5 < L < 20 R_S$ region, which occupy $\sim 50\%$ of the partial energetic particle pressure, but it is not entirely negligible in the case of H^+ as well (e.g., the polytropic index of H^+ is lower than $5/3$ throughout the $9.5 < L < 20$ region and lower than 1 closer to the planet). The addition and loss of plasma in the framework of different plasma beta conditions (e.g., Sergis et al., 2009) have an immediate impact on the plasma transport inside Saturn's magnetosphere. The characteristic energies of both H^+ and O^+ (see section 4) in conjunction with the suprathermal ion lifetimes due to charge exchange were rather revealing on this front, and together with the discussion presented here, we infer that the entropy (S) of the system cannot be conserved in Saturn's magnetosphere and will be found to decrease with decreasing distance from Saturn (at least for the $9.5 < L < 20$ region), as it happens at Earth's magnetotail (e.g., Erickson & Wolf, 1980).

Under the assumption of a collisionally isotropic gas, the entropy becomes a conserved quantity in purely adiabatic processes (where $S = T/n^{2/3}$, $\Gamma = 5/3$; cf. Borovsky & Cayton, 2011), which is not the case at Saturn's plasma sheet if we take into account both the H^+ and O^+ calculated polytropic indices. In principle, for a given system volume, V , and due to the fact that $\frac{dp}{dV}$ is proportional to $-\Gamma$, whereas $\frac{dT}{dV}$ is proportional to $1 - \Gamma$ (e.g., Livadiotis, 2016, Figure 1), the subadiabatic behavior of H^+ out beyond $9.5 R_S$ (where $\Gamma \sim 1.25$) implies that $\frac{dT}{dV} < 0$ and $\frac{dp}{dV} < 0$ (note that because $\Gamma < 1$ inside $9.5 R_S$, $\frac{dT}{dV} > 0$ for H^+). On the other hand, the quasi-isothermal behavior of O^+ implies that the temperature is constant and that $P \sim n$. A more practical example is given in the earlier analyses in Dialynas et al. (2009) where a typical suprathermal O^+ distribution, subjected to the neutral gas distribution around Saturn, was found to continuously cool down, resulting in no net gain in temperature as the particles move toward the planet to stronger magnetic fields.

At this point we need to emphasize again that our measurements include both a large number of energetic ion injections and *quiet* times and this simply indicates that the *polytropic relations* that we have derived here describe the particle distributions and the plasma sheet on average. In other words, these average results are some of the many generalized polytropic relations that depend on local energetic particle conditions, which may arise when studying more specialized cases. A typical example on this front involves the existence of transient flux tubes (so-called *blobs* or *bubbles*) at Earth, that impose local density and pressure enhancements which may affect the tail plasma population by resolving the pervasiveness of departures from the constant entropy and eliminate the violation of the pressure balance as described by Pontius and Wolf (1990; see also references therein).

Our measurements show indications that such a condition may be true for the Saturnian system as well, where ion injections, manifested in the partial pressure and density enhancements for both H^+ and O^+ in the outer parts of Saturn's magnetosphere, beyond $17 - 18 R_S$, may influence the *on average* plasma sheet conditions (e.g., see Figures 6 and 8). For example, the INCA camera on board Cassini revealed enhanced ENA emissions in both the dayside and nightside magnetosphere of Saturn that essentially form a rotating source of ENA emission (Carbary et al., 2008; Paranicas et al., 2005). These ENA emissions can be attributed to (quasi-)periodic injections that are reenergized approximately every Saturn rotation (Mitchell et al., 2009), that is, energetic particle blobs that are replenished only in certain local time sectors and otherwise decay because of charge exchange or longitudinal dispersion due to gradient and curvature drifts. Apparently, these injection events dominate the outer magnetosphere, producing the durable signatures observed in both the partial pressures and densities.

An additional complication to the processes explained above, especially in the night sectors at Saturn, where the magnetotail lies, is the loss of mass that has been shown to occur either through possible periodic (e.g., Cowley et al., 2015) or long-existing, rotating reconnection events (Yao et al., 2017), in the form of plasmoids (e.g., Jackman et al., 2014), or constantly from the postmidnight sector that is not necessarily related to reconnection (e.g., A. W. Smith et al., 2016). Despite the above complications, we infer that the calculated polytropic indexes for Saturn's plasma sheet, together with the semiempirical description of the major thermodynamical parameters for both suprathermal H⁺ and O⁺, can act as an invaluable input in recent models that aim to study the dynamics of Saturn's magnetosphere. In theory-driven studies, our results can be used in the method provided recently by Livadiotis (2018), to estimate the dynamical degrees of freedom in a plasma application, through the connection between the κ -index and the polytropic index.

Acknowledgments

The authors would like to thank J. Vandegriff (Johns Hopkins University Applied Physics Laboratory) for assistance with the MIMI data processing. We are grateful to all colleagues on the MIMI team, who provided valuable comments that have improved the presentation. Work at JHU/APL was supported by NASA under contracts NAS5-97271 and NNX07AJ69G and by subcontracts at the University of Maryland and the Office of Space Research and Technology of the Academy of Athens. The German contribution of MIMI/LEMMS was financed in part by the Bundesministerium für Bildung und Forschung (BMBF) through the Deutsches Zentrum für Luft- und Raumfahrt e.V. (DLR) and by the Max-Planck-Gesellschaft. Regoli, L. is supported by a NASA Living With a Star grant (NNX16AL12G). The Cassini/MIMI data and a user guide are available online through NASA's planetary data system (PDS-<https://pds-ppi.igpp.ucla.edu/mission/Cassini-Huygens/CO/MIMI>).

References

- Achilleos, N., Guio, P., & Arridge, C. S. (2010). A model of force balance in Saturn's magnetodisc. *Monthly Notices of the Royal Astronomical Society*, *401*, 2349–2371. <https://doi.org/10.1111/j.1365-2966.2009.15865.x>
- Allen, R. C., Mitchell, D. G., Paranicas, C. P., Hamilton, D. C., Clark, G., Rymer, A. M., et al. (2018). Internal versus external sources of plasma at Saturn: Overview from MIMI/CHEMS data. *Journal of Geophysical Research: Space Physics*, *123*, 4712–4727. <https://doi.org/10.1029/2018JA025262>
- Andriopoulou, M., Roussos, E., Krupp, N., Paranicas, C., Thomsen, M., Krimigis, S., et al. (2014). Spatial and temporal dependence of the convective electric field in Saturn's inner magnetosphere. *Icarus*, *229*, 57–70.
- Arridge, C. S., Khurana, K. K., Russell, C. T., Southwood, D. J., Achilleos, N., Dougherty, M. K., et al. (2008). Warping of Saturn's magnetospheric and magnetotail current sheets. *Journal of Geophysical Research*, *113*, A08217. <https://doi.org/10.1029/2007JA012963>
- Arridge, C. S., McAndrews, H. J., Jackman, C. M., Forsyth, C., Walsh, A. P., Sittler, E. C., et al. (2009). Plasma electrons in Saturn's magnetotail: Structure, distribution and energisation. *Planetary and Space Science*, *57*, 2032–2047.
- Azari, A. R., Liemohn, M. W., Jia, X., Thomsen, M. F., Mitchell, D. G., Sergis, N., et al. (2018). Interchange injections at Saturn: Statistical survey of energetic H⁺ sudden flux intensifications. *Journal of Geophysical Research: Space Physics*, *123*, 4692–4711. <https://doi.org/10.1029/2018JA025391>
- Baumjohann, W., & Paschmann, G. (1989). Determination of the polytropic index in the plasma sheet. *Geophysical Research Letters*, *16*(4), 295–298.
- Borovsky, J. E., & Cayton, T. E. (2011). Entropy mapping of the outer electron radiation belt between the magnetotail and geosynchronous orbit. *Journal of Geophysical Research*, *116*, A06216. <https://doi.org/10.1029/2011JA016470>
- Brandt, P. C., Dialynas, K., Dandouras, I., Mitchell, D. G., Garnier, P., & Krimigis, S. M. (2012). The distribution of Titan's high-altitude (out to ~50,000 km) exosphere from energetic neutral atom (ENA) measurements by Cassini/INCA. *Planet & Space Science*, *60*(1), 107–114.
- Brandt, P. C., Khurana, K. K., Mitchell, D. G., Sergis, N., Dialynas, K., Carbary, J. F., et al. (2010). Saturn's periodic magnetic field perturbations caused by a rotating partial ring current. *Geophysical Research Letters*, *37*, L22103. <https://doi.org/10.1029/2010GL045285>
- Brandt, P. C., Paranicas, C. P., Carbary, J. F., Mitchell, D. G., Mauk, B. H., & Krimigis, S. M. (2008). Understanding the global evolution of Saturn's ring current. *Geophysical Research Letters*, *35*, L17101. <https://doi.org/10.1029/2008GL034969>
- Carbary, J. F., Mauk, B. H., & Krimigis, S. M. (1983). Corotation anisotropies in Saturn's magnetosphere. *Journal of Geophysical Research*, *81*, 8937–8946.
- Carbary, J. F., & Mitchell, D. G. (2016). Seasonal variations in Saturn's plasma sheet warping. *Geophysical Research Letters*, *43*, 11957–11962. <https://doi.org/10.1002/2016GL071790>
- Carbary, J. F., Mitchell, D. G., Brandt, P., Roelof, E. C., & Krimigis, S. M. (2008). Statistical morphology of ENA emissions at Saturn. *Geophysical Research Letters*, *113*, A05210. <https://doi.org/10.1029/2007JA012873>
- Carbary, J. F., Paranicas, C., Mitchell, D. G., Krimigis, S. M., & Krupp, N. (2011). Energetic electron spectra in Saturn's plasma sheet. *Journal of Geophysical Research*, *116*, A07210. <https://doi.org/10.1029/2011JA016598>
- Christon, S. P., Hamilton, D. C., DiFabio, R. D., Mitchell, D. G., Krimigis, S. M., & Jontof-Hutter, D. S. (2013). Saturn suprathermal O₂⁺ and mass-28⁺ molecular ions: Long-term seasonal and solar variation. *Journal of Geophysical Research: Space Physics*, *118*, 3446–3462. <https://doi.org/10.1002/jgra.50383>
- Cowley, S. W. H., Nichols, J. D., & Jackman, C. M. (2015). Down-tail mass loss by plasmoids in Jupiter's and Saturn's magnetospheres. *Journal of Geophysical Research: Space Physics*, *120*, 6347–6356. <https://doi.org/10.1002/2015JA021500>
- Delamere, P. A., Bagenal, F., Dols, V., & Ray, L. C. (2007). Saturn's neutral torus versus Jupiter's plasma torus. *Geophysical Research Letters*, *34*, L09105. <https://doi.org/10.1029/2007GL029437>
- Delamere, P. A., Otto, A., Ma, X., Bagenal, F., & Wilson, R. J. (2015). Magnetic flux circulation in the rotationally driven giant magnetospheres. *Journal of Geophysical Research: Space Physics*, *120*, 4229–4245. <https://doi.org/10.1002/2015JA021036>
- Delcourt, D. C. (2002). Particle acceleration by inductive electric fields in the inner magnetosphere. *Atmospheric and Solar-Terrestrial Physics*, *64*(5-6), 551–559. [https://doi.org/10.1016/S1364-6826\(02\)00012-3](https://doi.org/10.1016/S1364-6826(02)00012-3)
- DiFabio, R. D. (2012). Spatial and temporal variations of the suprathermal (3-220 keV/e) ion composition in Saturn's equatorial magnetosphere, (PhD thesis). University of Maryland at College Park, College Park, MD.
- Dialynas, K., Brandt, P. C., Krimigis, S. M., Mitchell, D. G., Hamilton, D. C., Krupp, N., & Rymer, A. M. (2013). The extended Saturnian neutral cloud as revealed by global ENA simulations using Cassini/MIMI measurements. *Journal of Geophysical Research: Space Physics*, *118*, 3027–3041. <https://doi.org/10.1002/jgra.50295>
- Dialynas, K., Krimigis, S. M., Mitchell, D. G., Hamilton, D. C., Krupp, N., & Brandt, P. C. (2009). Energetic ion spectral characteristics in the Saturnian magnetosphere using Cassini/MIMI measurements. *Journal of Geophysical Research*, *114*, A01212. <https://doi.org/10.1029/2008JA013761>

- Dialynas, K., Paranicas, C. P., Carbary, J. F., Kane, M., Krimigis, S. M., & Mauk, B. H. (2017). Chapter 12—The kappa-shaped particle spectra in planetary magnetospheres. In G. Livadiotis (Ed.), *Kappa Distributions, Theory and Applications in Plasmas* (pp. 481–522). New York: Elsevier. <https://doi.org/10.1016/B978-0-12-804638-8.00012-7>
- Dougherty, M. K., Kellock, S., Southwood, D. J., Balogh, A., Smith, E. J., Tsurutani, B. T., et al. (2004). The Cassini magnetic field investigation. *Space Science Reviews*, *114*, 331–383.
- Dougherty, M. K., Khurana, K. K., Neubauer, F. M., Russel, C. T., Saur, J., Leisner, J. S., & Burton, M. E. (2006). Identification of a dynamic atmosphere at Enceladus with the Cassini magnetometer. *Science*, *311*, 1406–1409. <https://doi.org/10.1126/science.1120985>
- Erickson, G. M., & Wolf, R. A. (1980). Is steady convection possible in the Earth's magnetotail? *Geophysical Research Letters*, *7*, 897–900. <https://doi.org/10.1029/GL007i011p00897>
- Fok, M.-C., Moore, T. E., Brandt, P. C., Delcourt, D. C., Slinker, S. P., & Fedder, J. A. (2006). Impulsive enhancements of oxygen ions during substorms. *Journal of Geophysical Research*, *111*, A10222. <https://doi.org/10.1029/2006JA011839>
- Hapgood, M., Perry, C., Davies, J., & Denton, M. (2011). The role of suprathermal particle measurements in CrossScale studies of collisionless plasma processes. *Planetary and Space Science*, *59*, 618–629.
- Huang, C. Y., Goertz, C. K., Frank, L. A., & Rostoker, G. (1989). Observational determination of the adiabatic index in the quiet time plasma sheet. *Geophysical Research Letters*, *16*, 563.
- Jackman, C. M., Slavin, J. A., Kivelson, M. G., Southwood, D. J., Achilleos, N., Achilleos, N., et al. (2014). Saturn's dynamic magnetotail: A comprehensive magnetic field and plasma survey of plasmoids and traveling compression regions and their role in global magnetospheric dynamics. *Journal of Geophysical Research: Space Physics*, *119*, 5465–5494. <https://doi.org/10.1002/2013JA019388>
- Jia, X., & Kivelson, M. G. (2016). Dawn-dusk asymmetries in rotating magnetospheres: Lessons from modeling Saturn. *Journal of Geophysical Research: Space Physics*, *121*, 1413–1424. <https://doi.org/10.1002/2015JA021950>
- Jia, X., Kivelson, M. G., & Gombosi, T. I. (2012). Driving Saturn's magnetospheric periodicities from the upper atmosphere/ionosphere. *Journal of Geophysical Research*, *117*, A04215. <https://doi.org/10.1029/2011JA017367>
- Johnson, R. E., Fama, M., Liu, M., Baragiola, R. A., Sittler, E. C. Jr., & Smith, H. T. (2008). Sputtering of ice grains and icy satellites in Saturn's inner magnetosphere. *Planetary and Space Science*, *56*(9), 1238–1243. <https://doi.org/10.1016/j.pss.2008.04.003>
- Jurac, S., McGrath, M. A., Johnson, R. E., Richardson, J. D., Vasyliunas, V. M., & Eviatar, A. (2002). Saturn: Search for a missing water source. *Geophysical Research Letters*, *29*, 2172. <https://doi.org/10.1029/2002GL015855>
- Kane, M., Mitchell, D. G., Carbary, J. F., & Krimigis, S. M. (2014). Plasma convection in the nightside magnetosphere of Saturn determined from energetic ion anisotropies. *Planetary and Space Science*, *91*, 1–13.
- Kane, M., Mitchell, D. G., Carbary, J. F., Krimigis, S. M., & Cray, F. J. (2008). Plasma convection in Saturn's outer magnetosphere determined from ions detected by the Cassini INCA experiment. *Geophysical Research Letters*, *35*, L04102. <https://doi.org/10.1029/2007GL032342>
- Kennelly, T. J., Leisner, J. S., Gurnett, G. B., Hospodarsky, G. B., & Gurnett, D. A. (2013). Ordering of injection events within Saturnian SLS longitude and local time. *Journal of Geophysical Research: Space Physics*, *118*, 832–838. <https://doi.org/10.1002/jgra.50152>
- Khurana, K. K. (1997). Euler potential models of Jupiter's magnetospheric field. *Journal of Geophysical Research*, *102*, 11,295–11,306. <https://doi.org/10.1029/97JA00563>
- Khurana, K. K., Arridge, C. S., Schwarzl, H., & Dougherty, M. K. (2006). A model of Saturn's magnetospheric field based on latest Cassini observations. American Geophysical Union, Fall Meeting 2007, Abstract P44A-01. Retrieved from <http://adsabs.harvard.edu/abs/2006AGUSM.P44A.01K>
- Khurana, K. K., Mitchell, D. G., Arridge, C. S., Dougherty, M. K., Russell, C. T., Paranicas, C., et al. (2009). Sources of rotational signals in Saturn's magnetosphere. *Journal of Geophysical Research*, *114*, A02211. <https://doi.org/10.1029/2008JA013312>
- Kivelson, M. G. (2006). Does Enceladus govern magnetospheric dynamics at Saturn? *Science*, *311*, 1391–1392.
- Kollmann, P., Roussos, E., Kotova, A., Cooper, J. F., Mitchell, D. G., Krupp, N., & Paranicas, C. (2015). MeV proton flux predictions near Saturn's D ring. *Journal of Geophysical Research: Space Physics*, *120*, 8586–8602. <https://doi.org/10.1002/2015JA021621>
- Kollmann, P., Roussos, E., Paranicas, C., Krupp, N., Jackman, C. M., Kirsch, E., & Glassmeier, K.-H. (2011). Energetic particle phase space densities at Saturn: Cassini observations and interpretations. *Journal of Geophysical Research*, *116*, A05222. <https://doi.org/10.1029/2010JA016221>
- Krimigis, S. M., Carbary, J. F., Keath, E. P., Armstrong, T. P., Lanzerotti, L. J., & Gloeckler, G. (1983). General characteristics of hot plasma and energetic particles in the Saturnian magnetosphere: Results from the Voyager spacecraft. *Journal of Geophysical Research*, *88*, 8871–8892.
- Krimigis, S. M., Mitchell, D. G., Hamilton, D. C., Krupp, N., Livi, S., Roelof, E. C., et al. (2005). Dynamics of Saturn's magnetosphere from MIMI during Cassini's orbital insertion. *Science*, *307*, 1270–1273.
- Krimigis, S. M., Mitchell, D. G., Hamilton, D. C., Livi, S., Dandouras, J., Jaskulek, S., et al. (2004). Magnetospheric imaging instrument on the Cassini mission to Saturn/Titan. *Space Science Reviews*, *114*, 233–329. <https://doi.org/10.1007/s11214-004-1410-8>
- Krimigis, S. M., Sergis, N., Dialynas, K., Mitchell, D. G., Hamilton, D. C., Krupp, N., et al. (2009). Analysis of a sequence of energetic ion and magnetic field events upstream from the Saturnian magnetosphere. *Planetary and Space Science*, *57*, 1785–1794.
- Krimigis, S. M., Sergis, N., Mitchell, D. G., Hamilton, D. C., & Krupp, N. (2007). A dynamic rotating ring current around Saturn. *Nature*, *450*, 01053. <https://doi.org/10.1038/nature06425>
- Lindsay, B. G., & Stebbings, R. F. (2005). Charge transfer cross sections for energetic neutral atom data analysis. *Journal of Geophysical Research*, *110*, A12213. <https://doi.org/10.1029/2005JA011298>
- Livadiotis, G. (2016). Superposition of polytropes in the inner heliosheath. *The Astrophysical Journal-S*, *223*, 13. <https://doi.org/10.3847/0067-0049/223/1/13>
- Livadiotis, G. (2017). *Kappa Distributions: Theory and Applications in Plasmas*. New York: Elsevier.
- Livadiotis, G. (2018). Using kappa distributions to identify the potential energy. *Journal of Geophysical Research: Space Physics*, *123*, 1050–1060. <https://doi.org/10.1002/2017JA024978>
- Livadiotis, G., & McComas, D. J. (2009). Beyond kappa distributions: Exploiting Tsallis statistical mechanics in space plasmas. *Journal of Geophysical Research*, *114*, A11105. <https://doi.org/10.1029/2009JA014352>
- Livadiotis, G., & McComas, D. J. (2010). Exploring transitions of space plasmas out of equilibrium. *The Astrophysical Journal*, *714*, 971e987.
- Livadiotis, G., & McComas, D. J. (2012). Non-equilibrium thermodynamic processes: Space plasmas and the inner heliosheath. *The Astrophysical Journal*, *749*(11), 4.
- Mauk, B. H., Mitchell, D. G., McEntire, R. W., Paranicas, C. P., Roelof, E. C., Williams, D. J., et al. (2004). Energetic ion characteristics and neutral gas interactions in Jupiter's magnetosphere. *Journal of Geophysical Research*, *109*, A09S12. <https://doi.org/10.1029/2003JA010270>
- Mauk, B. H., Saur, J., Mitchell, D. G., Roelof, E. C., Brandt, P. C., Armstrong, T. P., et al. (2005). Energetic particle injections in Saturn's magnetosphere. *Geophysical Research Letters*, *32*, L14S05. <https://doi.org/10.1029/2005GL022485>
- Mitchell, D. G., Brandt, P. C., Carbary, J. F., Kurth, W. S., Krimigis, S. M., Paranicas, C., et al. (2015). Injection, interchange, and reconnection: Energetic particle observations in Saturn's magnetosphere. In A. Keiling, C. M. Jackman, & P. A. Delamere (Eds.), *Mag-*

- netotails in the Solar System, *Geophysical Monograph Series* (Chap. 19, vol. 207, pp. 327–343). Hoboken, NJ: John Wiley & Sons. <https://doi.org/10.1002/9781118842324.ch19>
- Mitchell, D. G., Brandt, P. C., Roelof, E. C., Dandouras, J., Krimigis, S. M., Mauk, B. H., et al. (2005). Energetic ion acceleration in Saturn's magnetotail: Substorms at Saturn? *Geophysical Research Letters*, *32*, L20501. <https://doi.org/10.1029/2005GL022647>
- Mitchell, D. G., Krimigis, S. M., Paranicas, C., Brandt, P. C., Carbary, J. F., Roelof, E. C., et al. (2009). Recurrent energization of plasma in the midnight-to-dawn quadrant of Saturn's magnetosphere, and its relationship to auroral UV and radio emissions. *Planetary and Space Science*, *57*, 1732–1742. <https://doi.org/10.1016/j.pss.2009.04.002>
- Newbury, J. A., Russell, C. T., & Lindsay, G. M. (1997). Solar wind polytropic index in the vicinity of stream interactions. *Geophysical Research Letters*, *24*, 1431–1434. <https://doi.org/10.1029/97GL01204>
- Nicolaou, G., & Livadiotis, G. (2016). Misestimation of temperature when applying Maxwellian distributions to space plasmas described by kappa distributions. *Ap&SS*, *959*, 361, 11, article id.359, 11 pp.
- Paranicas, C. P., Mitchell, D. G., Krimigis, S. M., Hamilton, D. C., Roussos, E., Krupp, N., et al. (2008). Sources and losses of energetic protons in Saturn's magnetosphere. *Icarus*, *197*, 519–525. <https://doi.org/10.1016/j.icarus.2008.05.011>
- Paranicas, C., Mitchell, D. G., Roelof, E. C., Brandt, P. C., Williams, D. J., Krimigis, S. M., & Mauk, B. H. (2005). Periodic intensity variations in global ENA images of Saturn. *Geophysical Research Letters*, *32*, 21. <https://doi.org/10.1029/2005GL023656>
- Paranicas, C. P., Mitchell, D. G., Roussos, E., Kollmann, P., Krupp, N., Müller, A. L., et al. (2010). Transport of energetic electrons into Saturn's inner magnetosphere. *Journal of Geophysical Research*, *115*, A09214. <https://doi.org/10.1029/2010JA015853>
- Paranicas, C. P., Thomsen, M. F., Achilleos, N., Andriopoulou, M., Badman, S. V., Hospodarsky, G., et al. (2016). Effects of radial motion on interchange injections at Saturn. *Icarus*, *264*, 342–351. <https://doi.org/10.1016/j.icarus.2015.10.002>
- Pilkington, N. M., Achilleos, N., Arridge, C. S., Guio, P., Masters, A., Ray, L. C., et al. (2015). Internally driven large-scale changes in the size of Saturn's magnetosphere. *Journal of Geophysical Research: Space Physics*, *120*, 7289–7306. <https://doi.org/10.1002/2015JA021290>
- Pontius, D. H. Jr., & Wolf, R. A. (1990). Transient flux tubes in the terrestrial magnetosphere. *Geophysical Research Letters*, *17*(1), 49–52.
- Porco, C. C., Helfenstein, P., Thomas, P. C., Ingersoll, A. P., Wisdom, J., West, R., et al. (2006). Cassini observes the active south pole of Enceladus. *Science*, *311*, 1393–1401.
- Press, W. H., Teukosky, S. A., Wetterling, W. T., & Flannery, B. P. (1992). *Numerical Recipes in C* (2nd ed.). Cambridge: Cambridge University Press.
- Regoli, L. H., Roussos, E., Dialynas, K., Luhmann, J. G., Sergis, N., Jia, X., et al. (2018). Statistical study of the energetic proton environment at Titan's orbit from the Cassini spacecraft. *Journal of Geophysical Research: Space Physics*, *123*, 4820–4834. <https://doi.org/10.1029/2018JA025442>
- Roelof, E. C., & Skinner, A. J. (2000). Extraction of ion distributions of magnetospheric ENA and EUV images. *Space Science Reviews*, *91*, 437–459.
- Roussos, E., Jones, G. H., Krupp, N., Paranicas, C., Mitchell, D. G., Lagg, A., et al. (2007). Electron microdiffusion in the Saturnian radiation belts: Cassini MIMI/LEMMS observations of energetic electron absorption by the icy moons. *Journal of Geophysical Research*, *112*, A06214. <https://doi.org/10.1029/2006JA012027>
- Roussos, E., Krupp, N., Paranicas, C. P., Kollmann, P., Mitchell, D. G., Krimigis, S. M., et al. (2011). Long- and short-term variability of Saturn's ionic radiation belts. *Journal of Geophysical Research*, *116*, A02217. <https://doi.org/10.1029/2010JA015954>
- Rymer, A. M., Mauk, B. H., Hill, T. W., André, N., Mitchell, D. G., Paranicas, C., et al. (2009). Cassini evidence for rapid interchange transport at Saturn. *Planetary and Space Science*, *57*, 1779–1784.
- Rymer, A. M., Mauk, B. H., Hill, T. W., Paranicas, C., André, N., Sittler, E. C., et al. (2007). Electron sources in Saturn's magnetosphere. *Journal of Geophysical Research*, *112*, A02201. <https://doi.org/10.1029/2006JA012017>
- Saur, J., Mauk, B. H., Kaßner, A., & Neubauer, F. M. (2004). A model for the azimuthal plasma velocity in Saturn's magnetosphere. *Journal of Geophysical Research*, *109*, A05217. <https://doi.org/10.1029/2003JA010207>
- Schippers, P., Blanc, M., André, N., Dandouras, I., Lewis, G. R., Gilbert, L. K., et al. (2008). Multi-instrument analysis of electron populations in Saturn's magnetosphere. *Journal of Geophysical Research*, *113*, A07208. <https://doi.org/10.1029/2008JA013098>
- Sergis, N., Jackman, C. M., Thomsen, M. F., Krimigis, S. M., Mitchell, D. G., Hamilton, D. C., et al. (2017). Radial and local time structure of the Saturnian ring current, revealed by Cassini. *Journal of Geophysical Research: Space Physics*, *122*, 1803–1815. <https://doi.org/10.1002/2016JA023742>
- Sergis, N., Krimigis, S. M., Mitchell, D. G., Hamilton, D. C., Krupp, N., Mauk, B. M., et al. (2007). Ring current at Saturn: Energetic particle pressure in Saturn's equatorial magnetosphere measured with Cassini/MIMI. *Geophysical Research Letters*, *34*, A05217. <https://doi.org/10.1029/2006GL029223>
- Sergis, N., Krimigis, S. M., Mitchell, D. G., Hamilton, D. C., Krupp, N., Mauk, B. M., et al. (2009). Energetic particle pressure in Saturn's magnetosphere measured with the Magnetospheric Imaging Instrument on Cassini. *Journal of Geophysical Research*, *114*, A02214. <https://doi.org/10.1029/2008JA013774>
- Shemansky, D. E., Liu, X., & Melin, H. (2009). The Saturn hydrogen plume. *Planetary and Space Science*, *57*, 1659–1670. <https://doi.org/10.1016/j.pss.2009.05.002>
- Smith, A. W., Jackman, C. M., & Thomsen, M. F. (2016). Magnetic reconnection in Saturn's magnetotail: A comprehensive magnetic field survey. *Journal of Geophysical Research: Space Physics*, *121*, 2984–3005. <https://doi.org/10.1002/2015JA022005>
- Smith, H. T., Johnson, R. E., Perry, M. E., Mitchell, D. G., McNutt, R. L., & Young, D. T. (2010). Enceladus plume variability and the neutral gas densities in Saturn's magnetosphere. *Journal of Geophysical Research*, *115*, A10252. <https://doi.org/10.1029/2009JA015184>
- Spence, E. H., & Kivelson, M. G. (1990). The variation of the plasma sheet polytropic index along the midnight meridian in a finite width magnetotail. *Geophysical Research Letters*, *17*, 591–594.
- Thomsen, M. F., Jackman, C. M., Tokar, R. L., & Wilson, R. J. (2014). Plasma flows in Saturn's nightside magnetosphere. *Journal of Geophysical Research: Space Physics*, *119*, 4521–4535. <https://doi.org/10.1002/2014JA019912>
- Thomsen, M. F., Roussos, E., Andriopoulou, M., Kollmann, P., Arridge, C. S., Paranicas, C. P., et al. (2012). Saturn's inner magnetospheric convection pattern: Further evidence. *Journal of Geophysical Research*, *117*, A09208. <https://doi.org/10.1029/2011JA017482>
- Thomsen, M. F., Tokar, R. J., Wilson, R. L., Reisenfeld, B., & Jackman, C. M. (2013). Cassini/CAPS observations of duskside tail dynamics at Saturn. *Journal of Geophysical Research: Space Physics*, *118*, 5767–5781. <https://doi.org/10.1002/jgra.50552>
- Vasyliunas, V. M. (1968). A survey of low-energy electrons in the evening sector of the magnetosphere with OGO 1 and OGO 3. *Geophysical Research Letters*, *73*, 2839–2884.
- Vasyliunas, V. M. (2008). Comparing Jupiter and Saturn: Dimensionless input rates from plasma sources within the magnetosphere. *Annales Geophysicae*, *26*, 1341–1343.

- Wilson, R. J., Bagenal, F., Delamere, P. A., Desroche, M., Fleshman, B. L., & Dols, V. (2013). Evidence from radial velocity measurements of a global electric field in Saturn's inner magnetosphere. *Journal of Geophysical Research: Space Physics*, *118*, 2122–2132. <https://doi.org/10.1002/jgra.50251>
- Wilson, R. J., Bagenal, F., & Persoon, A. M. (2017). Survey of thermal plasma ions in Saturn's magnetosphere utilizing a forward model. *Journal of Geophysical Research: Space Physics*, *122*, 7256–7278. <https://doi.org/10.1002/2017JA024117>
- Wing, S., & Johnson, J. R. (2010). Introduction to special section on entropy properties and constraints related to space plasma transport. *Journal of Geophysical Research*, *115*, A00D00. <https://doi.org/10.1029/2009JA014911>
- Yao, Z. H., Coates, A. J., Ray, L. C., Rae, I. J., Grodent, D., Jones, G. H., et al. (2017). Corotating magnetic reconnection site in Saturn's magnetosphere. *The Astrophysical Journal Letters*, *846*, L25. <https://doi.org/10.3847/2041-8213/aa88af>
- Young, D. T., Berthelier, J.-J., Blanc, M., Burch, J. L., Bolton, S., Coates, A. J., et al. (2005). Composition and dynamics of plasma in Saturn's magnetosphere. *Science*, *307*, 1262–1266. <https://doi.org/10.1126/science.1106151>